Fall 2019

Improving Paper-Based Microfluidic Mixing With the Incorporation of Flow Disrupting Structures

Hannah C. Green

IMPROVING PAPER-BASED MICROFLUIDIC MIXING WITH THE INCORPORATION OF FLOW DISRUPTING STRUCTURES

by

Hannah C. Green, B.S.

A Thesis Presented in Partial Fulfillment
of the Requirements of the Degree
Master of Science

COLLEGE OF ENGINEERING AND SCIENCE
LOUISIANA TECH UNIVERSITY

November 2019

LOUISIANA TECH UNIVERSITY

GRADUATE SCHOOL

September 20, 2019
Date of thesis defense

We hereby recommend that the thesis prepared by

Hannah C. Green

entitled IMPROVING PAPER-BASED MICROFLUIDIC MIXING WITH THE INCORPORATION OF FLOW DISRUPTING STRUCTURES

be accepted in partial fulfillment of the requirements for the degree of

Master of Science in Engineering, Biomedical Engineering Concentration

Dr. Bryant Hollins, Supervisor of Thesis Research

Dr. Steven Jones,
Head of Biomedical Engineering

Members of the Thesis Committee:
Dr. Bryant Hollins
Dr. Steven Jones
Dr. Gergana Nestorova

Approved:

Hisham Hegab
Dean of Engineering & Science

Approved:

Ramu Ramachandran
Dean of the Graduate School

GS Form 13
(01/19)

ABSTRACT

Paper-based microfluidic devices provide a light-weight, cost effective platform for diagnostic and analytical testing. The goal of this project is to enhance paper-based microfluidic mixing by incorporating fluid flow disrupting structures (referred to here as rib bones) into the microdevice design to expand the analytical capabilities of paper-based microfluidic devices. The devices are fabricated on Whatman CHR-1 chromatography paper. The devices are designed in SolidWorks and printed using a solid ink printer (ColorQube 8580). The wax is penetrated into the paper to create hydrophobic barrier regions by heating in a convection oven until the wax is fully penetrated. The parameters of the rib bone structure that were evaluated include the width of the individual rib bone (α), the spacing between the rib bones (β), and the angle of the inlet junction into the mixing channel (γ). The mixing efficiency was characterized by how well two fluids of differing colors mixed over a constant length mixing channel. The solution used for mixing is a 1:4 v/v isopropyl alcohol:water ratio with 10 drops of food coloring added for the color. Yellow and blue food coloring, which mix to form green, were used for the experiments. To quantify the effectiveness of the mixing, a digital image of the device was taken, and MATLAB was used to determine the RGB color code of the area distal to the rib bones. The outcome of this project is a fully defined mixing channel design that can be incorporated into other paper-based microfluidic designs.

APPROVAL FOR SCHOLARLY DISSEMINATION

The author grants to the Prescott Memorial Library of Louisiana Tech University the right to reproduce, by appropriate methods, upon request, any or all portions of this Thesis. It is understood that "proper request" consists of the agreement, on the part of the requesting party, that said reproduction is for his personal use and that subsequent reproduction will not occur without written approval of the author of this Thesis. Further, any portions of the Thesis used in books, papers, and other works must be appropriately referenced to this Thesis.

Finally, the author of this Thesis reserves the right to publish freely, in the literature, at any time, any or all portions of this Thesis.

Author _____

Date _____

DEDICATION

This thesis is dedicated to my family for their love and support throughout all of my schooling and educational exploits.

TABLE OF CONTENTS

LIST OF FIGURES

LIST OF TABLES

ACKNOWLEDGMENTS

Thank you to my committee Dr. Bryant Hollins, Dr. Steven Jones, and Dr. Gergana Nestorova, and thanks to Dr. Kevin Holly.

CHAPTER 1

INTRODUCTION

The goal of this project is to improve paper-based microfluidic mixing by incorporating fluid flow disrupting structures into the microfluidic device design. This project will be the first step towards developing a functional mixing design that can be incorporated into any paper-based microfluidic device. Currently, the hydrophobic barriers that form the hydrophilic channels of paper-based microfluidic are mostly used to guide the fluid from inlets to one or more test regions that contain the reagents and chemicals. Use of the hydrophobic barriers to be more than just fluid transporting channels could greatly expand the capabilities of paper-based devices. The hydrophobic material can be used as obstacles within the channel, which would facilitate the mixing of two fluids within the channel and produce a completely homogeneous mixture at the end of the channel.

Successful completion of this project would enable the design of a robust paper-based ELISA platform. ELISA (enzyme-linked immunosorbent assay) is a plate-based assay technique designed to detect and quantify substances such as peptides, proteins, antibodies and hormones. ELISAs are typically performed in 96-well polystyrene plates, which passively bind antibodies and proteins [1]. This current method is that it can required up to 6 hours of incubation time to allow the antibodies to bind with the

proteins, and it can require to 100 μL of sample volume. Microfluidic ELISA assays have already been developed that significantly reduce the incubation time and sample volume needed for testing, but a paper-based ELISA could further reduce the time and sample volume and reduce fabrication and deployment costs [2].

1.1 Hypothesis

Fluidic mixing can be improved within paper-based microfluidic devices through channel design and the incorporation of flow disrupting structures within the channels of the devices compared to unobstructed channels. I investigated this hypothesis by pursuing two Specific Aims. They are to determine the parameters of the flow-disrupting lines for optimal paper-based microfluidic mixing and to evaluate the effects of the microfluidic device design parameters on paper-based microfluidic mixing.

1.1.1 Specific Aim 1

Specific Aim 1 is to determine the parameters of the flow-disrupting lines for optimal paper-based microfluidic mixing. Aim 1 focuses on the optimization of the flow-disrupting structure parameters including the thickness of each line (α), the spacing between the lines (β), and the angle of the inlet channel (γ). Optimizing these parameters while provide the best possible fluidic mixing using the flow disrupting line design and inlet angle manipulation.

1.1.2 Specific Aim 2

Specific Aim 2 is to evaluate the effects of the microfluidic device design parameters on paper-based microfluidic mixing. Aim 2 will focus on the quantification of the evaluation method of the mixing efficiency. Since the results of mixing are determined from the resultant color of green produced when mixing yellow and blue

fluids, a quantification method will be developed to accurately determine the level of mixing.

1.2 Overview

This chapter is a brief overview of the project and its objectives. This thesis contains six chapters. In Chapter 2, an in-depth review of the current literature in the field is presented, along with key knowledge and technical gaps identified. In Chapter 3, a detailed description of the project's methodology and materials is given. Chapter 4 contains the elements of the device design including the reproducibility and design limitations of the devices. Chapter 5 contains the device testing of the mixing efficiency of each device parameter. Chapter 6 is the conclusion and future plans of this work.

CHAPTER 2

BACKGROUND AND LITERATURE REVIEW

2.1 Microfluidics

Microfluidics deal with the flow of fluids through micrometer size channels. For something to be considered microfluidic, only one dimension of the channel must be in the micrometer range, usually considered to be less than 100 μm [3]. Microfluidic devices are the platforms made to perform these microfluidic functions. The channels of microfluidic devices are designed to mix, pump, dilute, or transport the sample fluid [3] [4] [5] [6] [7]. These devices work with microliter sized samples, while still providing accurate results [8]. The reagents needed for the desired tests are placed in the channels or reservoirs, and once the sample fluid makes contact with the reagents, the reaction and the results can then be read. Many microfluidic devices are biocompatible, allowing test to be run with biological fluids [9]. Some devices have also been developed for protein and DNA analysis, as well as cell cultivation and proliferation [10] [11] [12]. These devices can be fabricated from various substrates, including silicon, glass, chromatography paper, and polymers such as polydimethylsiloxane (PDMS), polymethyl methacrylate (PMMA), and polycarbonate (PC) [6] [13] [14]. Representative microfluidic devices can be seen in Figure 2-1, which shows the diverse substrates possible for device design.

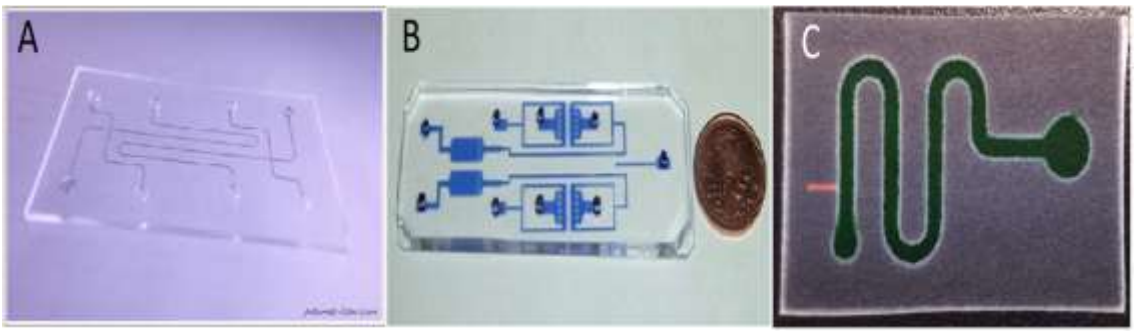

Figure 2-1: (A) PMMA microfluidic device [15], (B) PDMS microfluidic device [16], and (C) Paper-based microfluidic device.

2.1.1 History

Microfluidics was born out of the need to miniaturize computer technology in order to bring them to space. This need led to the development of the first microprocessors and semiconductors, which required micromanufacturing techniques to produce, particularly the use of silicon etching [3]. This technology allowed the integration of mechanical micro-elements on a silicon wafer. This new type of device became known as a Micro Electro Mechanical Systems (MEMS) device. The first commercially available MEMS devices were the nozzles used for inkjet printers [17]. From there, researchers investigated the applications of MEMS devices in biology, chemistry and biomedical fields [3]. These applications required the movement and control of fluids, which lead to the development of microfluidics. The majority of microfluidic devices were initially made from silicon and glass, using the micromachining methods borrowed from the semiconductor industry.

Paper-based microfluidic devices were first introduced by Martinez et al. in 2007 out of the Whitesides Research Group. Martinez et al. used SU-8 2010 photoresist to fabricate a hydrophobic patterned paper device. The paper was then spun, baked, exposed

to a UV-light with a mask, and then baked again [18]. This created the hydrophobic walls within the hydrophilic paper substrate. Martinez et al. tested their device using a colorimetric detection for both glucose and protein in urine. The photoresist successfully kept the sample fluid within the channels of the device and the intensity of the color increased as the concentrations of the glucose and protein increased within the artificial urine sample.

2.1.2 Common Fabrication Methods

Microfluidic devices can be fabricated using many different methods. Each method was developed to be faster, more cost effective, and have a higher resolution than the last method. Some of the more common fabrication methods for microfluidic devices includes photolithography, hot embossing, and 3D printing.

2.1.2.1 Photolithography

Photolithography is a common method of fabrication for many microfluidic substrates. Photolithography works by selectively exposing photoresist to ultraviolet (UV) light. The UV light is shone through what is called a photomask which blocks the UV light from reaching the photoresist in the desired pattern [14] [19]. Before the UV light exposure, the photoresist is first poured onto a flat substrate and then spun to level out the photoresist and make sure it is all one consistent thickness [19]. Photoresist can be positive or negative. The positive photoresist becomes soluble when exposed to the UV light, and can be washed away, leaving what was not exposed to the light [14]. Negative photoresist becomes insoluble once exposed to the UV light, leaving what was not exposed to be washed away [14]. The most common negative photoresist is SU-8 due to

its biocompatibility [20]. Figure 2-2 shows the photolithography process with positive and negative photoresist.

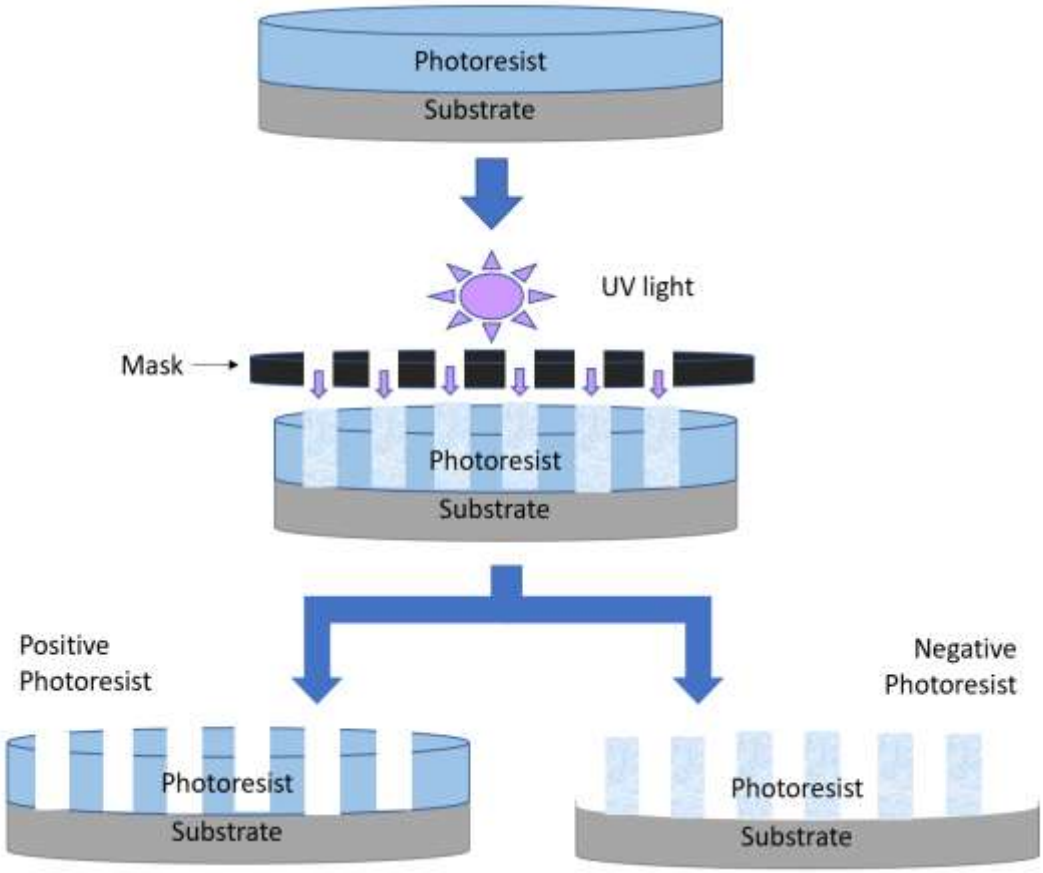

Figure 2-2: Fabrication process for photolithography with positive and negative photoresist.

For soft lithography, the photoresist method is used to make a silicon mold, which is then used to make a PDMS stamp on which the desired patterning material is coated and transferred to a substrate through microstamping [6] [14]. Multiple replica PDMS stamps can be made from a single silicon mold. The silicon molds are made using the traditional photolithography process and then the PDMS is poured into the mold and allowed to cure [21].

2.1.2.2 Hot Embossing

Hot embossing is another common microfluidic fabrication method used for thermoplastic polymers such as PMMA, PC, and polyvinylchloride (PVC) [6]. Hot embossing involves heating a metal or silicon mold to the glass transition temperature of the polymer to be imprinted, and then pressing it to the polymer. The material under the mold is displaced and the microchannels are formed [6]. Hydraulic presses are used to create the pressure needed at the glass transition temperature to reshape the polymers [22]. Figure 2-3 depicts the process of hot embossing with a mold and a polymer.

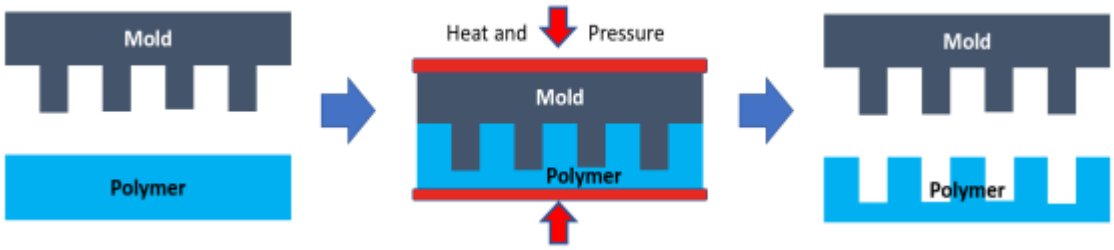

Figure 2-3: Fabrication process for hot embossing.

2.1.2.3 3D Printed Microfluidics

3D printed microfluidics came into existence in the late 1990s and have be on the rise since 2013 [23]. 3D printing is an inexpensive alternative to the photolithography methods used for silicon and soft lithography methods used for PDMS. 3D-printed microfluidic devices have so far been functionalized for DNA separation [24], cell culturing in transparent bio-microfluidic devices [25], microparticle separation, and fluidic mixing [26], among others. Current microfluidic 3D printing techniques include stereolithography (SLA), digital micromirror device-based projection printing (DMD-PP), two-photon polymerization (2PP), fused deposition modelling (FDM), and inkjet

[27]. SLA uses a focused UV laser to selectively harden a layer of photopolymer resin [28]. Once that layer is cured, another layer of resin is deposited and then selectively hardened. The process continues until the device is complete. DMD-PP projects a laser light using a controllable digital mirror [27]. This allows the laser light the cure an entire layer at one time. DMD-PP is considered a high-throughput 3D manufacturing technique that can obtain micrometer resolution [29]. 2PP uses femtosecond laser pulses to cure photosensitive resin [27] [30]. It allows the laser to cure in a volume of photosensitive material instead of curing layer by layer. FDM heats thermoplastics to a semisolid state and then extrudes it out of a nozzle [27]. As it extrudes, it cools and solidifies into the shape it was placed. This is also a layer by layer method [31]. Inkjet 3D printing uses a similar method to normal inkjet printing, but instead of extruding ink, these printers extrude photoresin, wax, PMMA, and silver nanoparticle ink [27] [32]. Once a layer is printed and cured, the build tray is lowered for the next layer to be constructed. Figure 2-4 show a 3D printed device using poly(ethylene glycol) diacrylate (PEG-DA) and SLA fabrication.

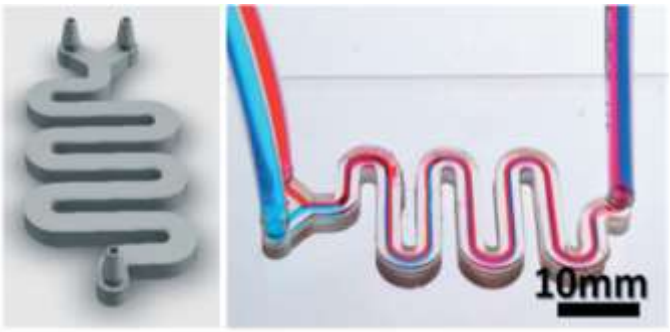

Figure 2-4: 3D printed device using poly(ethylene glycol) diacrylate (PEG-DA) and SLA fabrication [25].

2.2 Microfluidic Paper-based Analytical Devices

Microfluidic paper-based analytical devices (µ-PADs) are low cost, light weight, simplistic point of care devices [33]. µ-PADs are created from a hydrophilic membrane, usually chromatography paper, that has been patterned with a hydrophobic material to create hydrophilic channels to control the fluid flow. The desired reagents for functionality are placed and dried within the hydrophilic regions that would cause a reaction with the sample fluid when the fluid reached the chemicals through capillary action.

Paper-based devices are most commonly used for simple yes/no type of testing in fluidic samples. Colorimetric detection uses enzymatic or chemical color change reactions to produce a qualitative yes/no output using a visual color change that can be seen with the naked eye. Colorimetric detection can be a color change or a change in intensity of a single color [34] [35]. Three other reported detection methods for paper-based microfluidic devices have both advantages and disadvantages over colorimetric, as discussed below. These methods are electrochemical (EC), chemiluminescence (CL) and electrochemiluminescence (ECL) detection [6].

EC uses an external electrical device to detect a chemical reaction between the reactants and test sample. EC detection can detect and quantify the presence of analytes, with sensitivity in the nanomolar (nM) range [36]. In 2010, Nie et al. developed multiple electrochemical microfluidic analytical devices (EµPADs) that use a commercially available glucometer. Nie et al. were able to replicate the meters test strip design, made of plastic, on paper by using wax printing for the hydrophobic barriers, silver ink for the needed wires and graphite ink for the internal reference electrodes [37]. With this setup,

they were able to test for glucose, lactate, and cholesterol in human plasma or whole blood and ethanol in an aqueous solution [37]. In 2018, Suresh et al. developed an EμPAD for ultra-low detection of urea using a two-electrode setup [38]. Suresh et al. also used wax printing to create the hydrophobic barriers and silver contacts for the electrodes. The enzyme catalyst urease was used to hydrolyze the urea. The reaction produces ammonium carbonate which dissociated into several ions which are measured by the electrodes [38].

CL detection involves an associative chemiluminescence reaction that is triggered from the products of the initial analyte reaction. The luminescence is detected and recorded using a luminescence analyzer equipped with a photomultiplier. In 2011, Yu et al. developed a microfluidic paper-based chemiluminescence analytical device (μPCAD) that detects glucose and uric acid simultaneously. [39]. Glucose oxidase and urate oxidase were used respectively to oxidize the samples and then trigger the chemiluminescence reaction between rhodamine derivative and the generated hydrogen peroxide [39].

ECL detection combines the chemiluminescence detection method with an electrochemical detection device. In 2011, Delaney et al. developed an electrochemiluminescent paper-based microfluidic device for detection of 2-(dibutylamino)- ethanol (DBAE) and nicotinamide adenine dinucleotide (NADH) using an orange luminescence caused by tris(2,20 -bipyridyl)ruthenium(II) ($Ru(bpy)_3^{2+}$). Delaney et al. use a mobile phone camera to act as the photodetector and to capture an image of the luminescencing device. The images were then analyzed in a program written in Python [40]. The work by Delaney et al. showcased how simple, off-the-shelf products

that are readily available could be integrated to advance analytical detection and sensitivity in µ-PAD technology.

Though EC, CL, and ECL detection methods help paper-based device reach a new level of sensitivity, all of these methods require an external device to read the results. Although Nie et al. utilized a commercially available, cost effective, and portable glucometer for their EµPAD, that is not usually the case. Many of these detection methods still need larger electronic systems available to read the results, such as cameras and computers. These factors can be considered limitations, but it will still depend on the application of the device and where the device is intended to be used. For example, in common academic settings where benchtop prototypes are being fabricated, bulky external detection methods are not considered a significant limitation; however,in point-of-care, rapidly deployable systems they become an almost insurmountable burden.

2.2.1 Paper-Based Fabrication Techniques

Through their rise in popularity, many fabrication methods for paper-based microfluidic devices have been developed. The goal for every fabrication method is to create low-cost, high resolution devices. Some fabrication techniques include wax screen printing, laser printing, and wax printing.

2.2.1.1 Wax Screen Printing

Wax Screen printing requires a patterned screen and solid wax. The wax is rubbed through the screen onto the paper in the patterned opening in the screen. The paper is then heated using a hot plate to melt the wax through the paper and create the hydrophobic barriers. Figure 2-5 shows a schematic of the wax screen printing fabrication process.

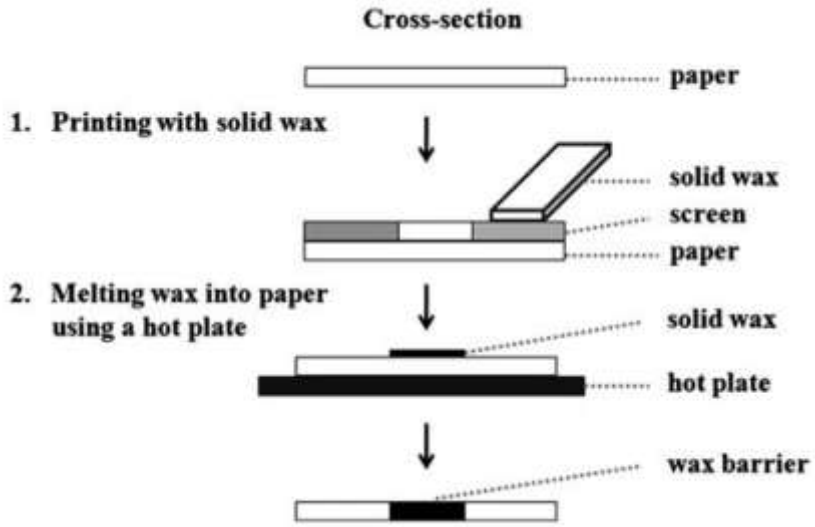

Figure 2-5: Schematic of the fabrication process of paper-based microfluidic devices using the wax screen printing method [41].

Although this method is highly cost effective, it has the least amount of resolution, creating hydrophobic barriers around 1200-1800 µm and the hydrophilic channels around 550 – 1000 µm [41].

2.2.1.2 Laser Printer

A new method for paper-based microfluidic device fabrication from Ghosh et al. uses a commercially available laser printer to fabricate high-resolution microfluidic devices on paper (Figure 2-6) [42]. This method uses the hydrophobic toner ink to pattern the paper to create the channels. Once the toner ink is printed on the paper, it is heated in an oven to melt the toner ink through the paper. After heating, the device is ready to be functionalized. This method has good resolution, only needing printed line of 200 µm to block flow.

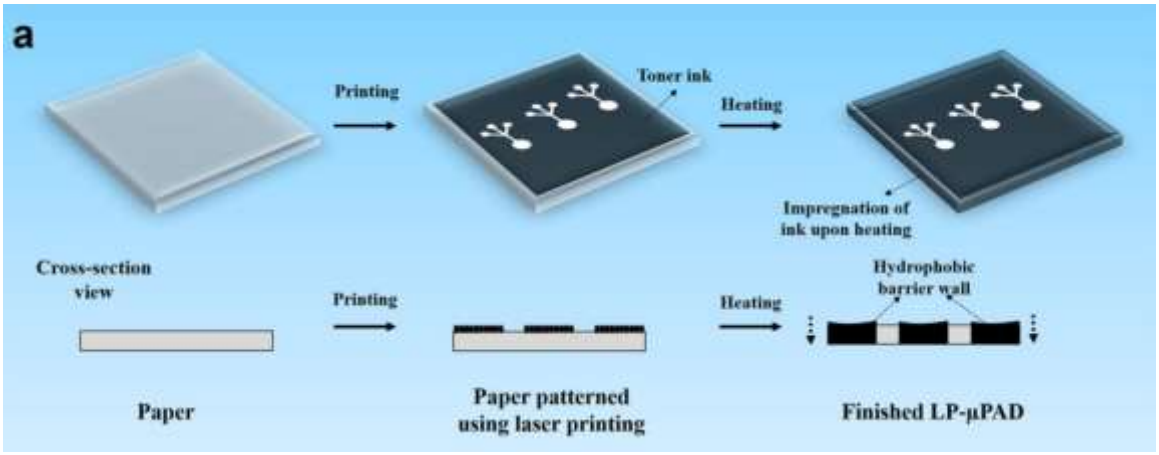

Figure 2-6: Schematic of the fabrication process of paper-based microfluidic devices using a laser printer for hydrophobic barrier patterning [42].

2.2.1.3 Wax Printing

A popular paper-based microfluidic fabrication technique is wax printing (Figure 2-7). The process uses a solid ink wax printer, which operates similarly to an ink jet printer, but deposits wax instead of in on the paper The wax is then heated on the paper to melt the wax through the paper, usually in a convection oven or on a hot plate [43]. Once the wax melts completely through the paper, the device is ready to be functionalized with any reagents. Carrilho et al. determined that wax printing required a minimum barrier of 300 µm to fully block fluid flow [13].

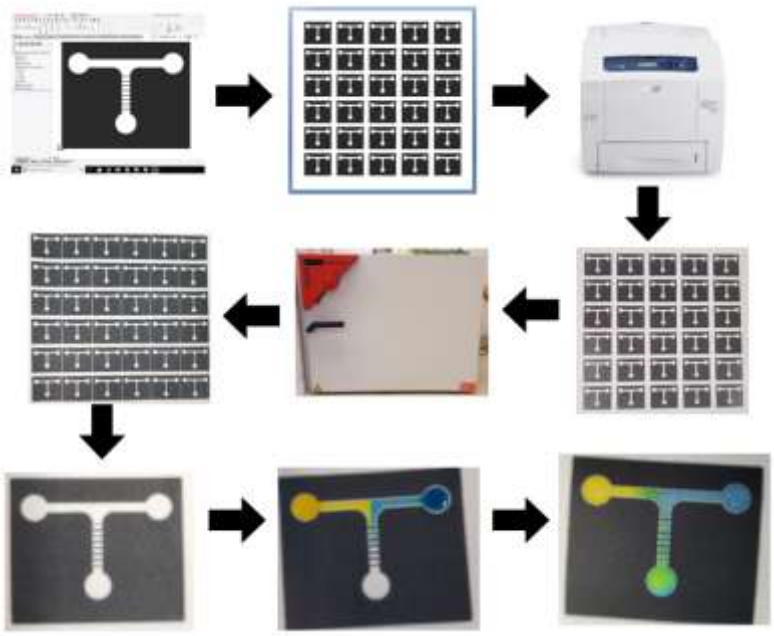

Figure 2-7: Fabrication Process for paper-based microfluidic devices using a solid ink wax printer.

2.2.2 Lateral Flow Assays

Lateral flow assays (LFA) are a popular type of paper-based microfluidic device that use capillary action to drive the fluid flow across the test regions [44]. The standard LFA has four parts: a sample pad, the conjugate pad, the reaction membrane and the absorbent pad [45]. The sample to be tested is dropped onto the sample pad. The labeled tags are combined with biorecognition elements on the conjugate pad [45]. The antigen-antibody interactions take place on test and control lines on the reaction membrane, which is usually made using nitrocellulose membrane [45]. The absorbent pad absorbs the excess sample is taken up by the absorbent pad, the sample is transferred from each part using capillary action.

The most common LFA is the at home pregnancy test, which tests for the human chorionic gonadotropin (hCG) in an individual's urine. hCG is a hormone secreted by the

developing placenta after fertilization and can be found in the blood and urine [14] [46]. The test uses the capillary action of the porous materials to drive the sample to the conjugate pad, which contains mouse monoclonal anti-hCG antibody-enzyme conjugates. The sample then flows to the test region of the reaction membrane that contains immobilized polyclonal anti-hCG antibodies and a dye substance [14]. The sample then flows to the control strip in the reaction membrane that contains immobilized goat anti-mouse antibodies and the same dye as the test strip [14]. The immobilized enzymes activate the dye in the test region if hCG is present in the sample and in the control strip.

2.2.3 Some Applications of Paper-Based Microfluidics

The applications of paper-based microfluidic devices have grown tremendously since Martinez et al. created the first paper-based test for glucose and protein in an artificial urine sample. Some devices have been developed to test for heavy metals such as mercury (III), copper (II), lead (II), and nickel (II) [34]. A colorimetric paper-based device has also been developed for detection of nitrates and nitrites using Griess reagent [47]. Heavy metal and nitrate/nitrite testing are important for water quality testing. As stated above, EC, CL, and ECL detection devices have been developed for glucose, urea, uric acid, lactate and cholesterol detection. These examples are by no means exhaustive, and paper-based microfluidic device applications continue to grow.

2.3 Mixing Limitations

One of the many challenges of developing and designing microfluidic devices is effectively mixing samples for reactions and/or detection. This is a challenge because all microfluidic devices inherently have low Reynolds Number flow regimes [4]. This limitation requires devices to be created that are sufficiently long to ensure adequate

mixing, but an increase in length results in an increase in analysis times. This project is attempting to decrease analysis times by increasing mixing efficiencies in microfluidic devices.

2.3.1 Polymeric Mixing

Much time and effort has been put into creating mixing flow patterns in polymeric devices [4]. Some established methods for mixing in polymeric devices include splitting the fluid flow and then recombining it, incorporating vortex-type micromixers, mixing fluids with bubbles, and altering device designs from straight to curved (serpentine) channels [4] [48]. However, little effort to achieve homogeneous mixing has been put forth for paper-based microfluidic devices.

2.3.2 Current Paper-Based Mixing

In 2012, Rezk et al. used 30 MHz surface acoustic waves (SAW) to achieve homogenous mixing within a paper-based microfluidic device, as shown in Figure 2-8 [49]. Rezk et al. developed a SAW device that attaches to the end of the channel to directly deliver the SAW to the paper channel.

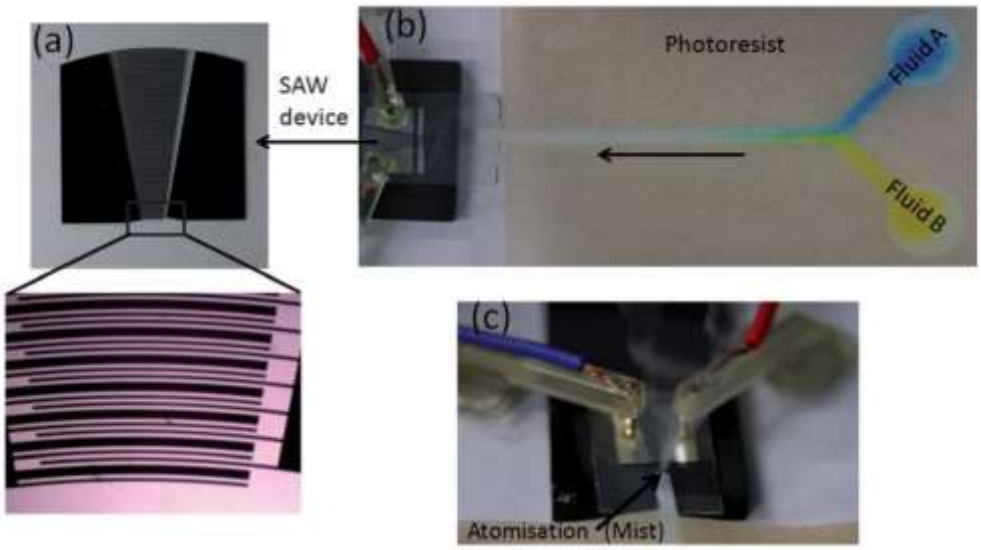

Figure 2-8: (A) Image of the focused SPUDT (Single-Phase Unidirectional Surface Acoustic Transducer) across which an oscillating RF signal is applied to generate the SAWs that act to draw flow through the paper microfluidics device. (B) The end of the flow channel at the edge of the paper is placed at the focal point of the SAW such that (C) the atomisation of the fluid out of the channel at the paper edge draws liquid through the Y-channel from its two reservoirs [49].

Although Rezk et al. were successful, their procedure required an external device, and thus there is still room for improvement to produce homogeneously mixed fluids within µ-PADs without use of an external device.

CHAPTER 3

MATERIALS AND METHODS

3.1 Device Fabrication Process

3.1.1 Design

The device designs are created and edited in Solidworks to allow for accurate dimensions. All devices with a zero-degree inlet angle (γ) are 25×30 mm and all devices with an inlet angle greater than zero are 30×30 mm devices. The inlet reservoirs are circles with a 2.5 mm radius and all channels are 2 mm in width. Figure 3-1 depicts one of the device designs. Labels indicate either design parameters that will be varied to optimize the mixing of the devices or dimensions for the constants between each device design.

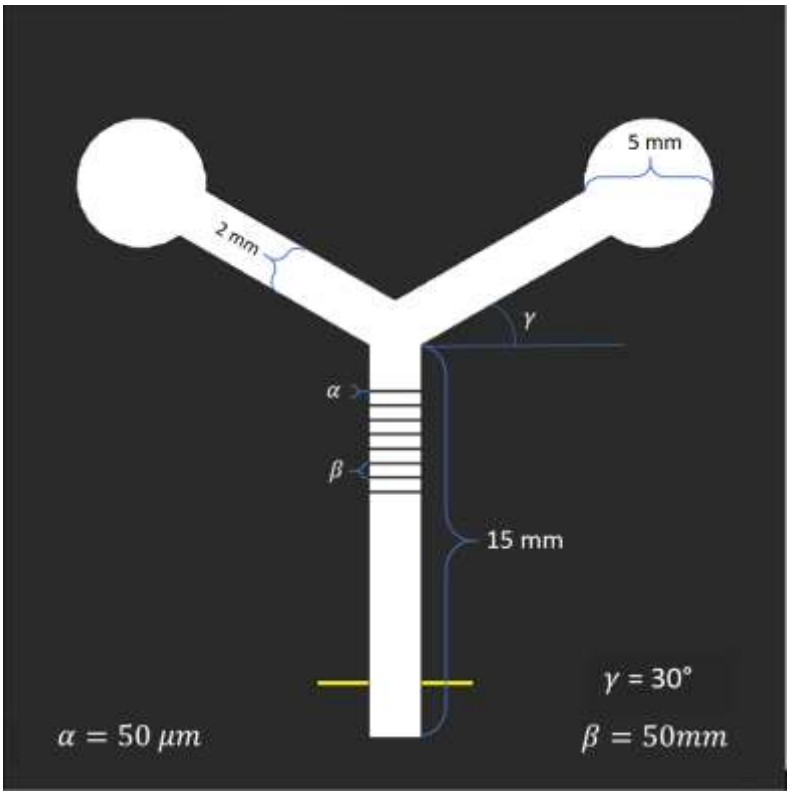

Figure 3-1: Solidworks design of the microfluidic mixing device with 50 µm flow disrupting structures thickness (α) and 50 mm spacing (β). The angle of the two in inlet channels (γ) is 30°. The mixing channel for all the designed devices is 15 mm. The channel width throughout the devices is 2 mm and the inlet reservoir circles are 5 mm in diameter.

The devices are created in Solidworks, saved as TIF images, and imported into Microsoft office word. Once in word, the device images are cropped and sized back down to their original dimensions. Multiple copies are then made on the sheet.

3.1.2 Printing and Heating

The devices are printed using the ColorQube 8580 solid ink printer. They are printed in melted wax on Whatman CHR-1 chromatography paper, as scaled on the word document. After the devices are printed, the sheet of devices is then heated in a convection oven. The oven melts wax and allows it to flow through the paper, ensuring that the wax barriers penetrate through the thickness of the paper. The devices are heated

at 80 °C in the oven for 6 – 8 minutes, or until the wax is fully penetrated through the paper. After the sheet of devices is fully penetrated, it can be cut into the individual devices, which are then ready for testing.

3.2 Device Testing

3.2.1 Color Solution

The color solutions used for testing were a 1:4 v/v isopropyl alcohol:water ratio with 10 drops of food coloring added for the color. The alcohol was added to the solution to help dilute the food coloring and to ensure the water does not separate from the food coloring while flowing through the chromatography paper. Yellow and blue food coloring were chosen to mix and form green.

3.2.2 Mixing on Devices

Each device was placed on pegs at each corner to suspend the device in the air. This allowed the fluid to flow through the channel, uninhibited by contact from the table surface as shown in Figure 3-2.

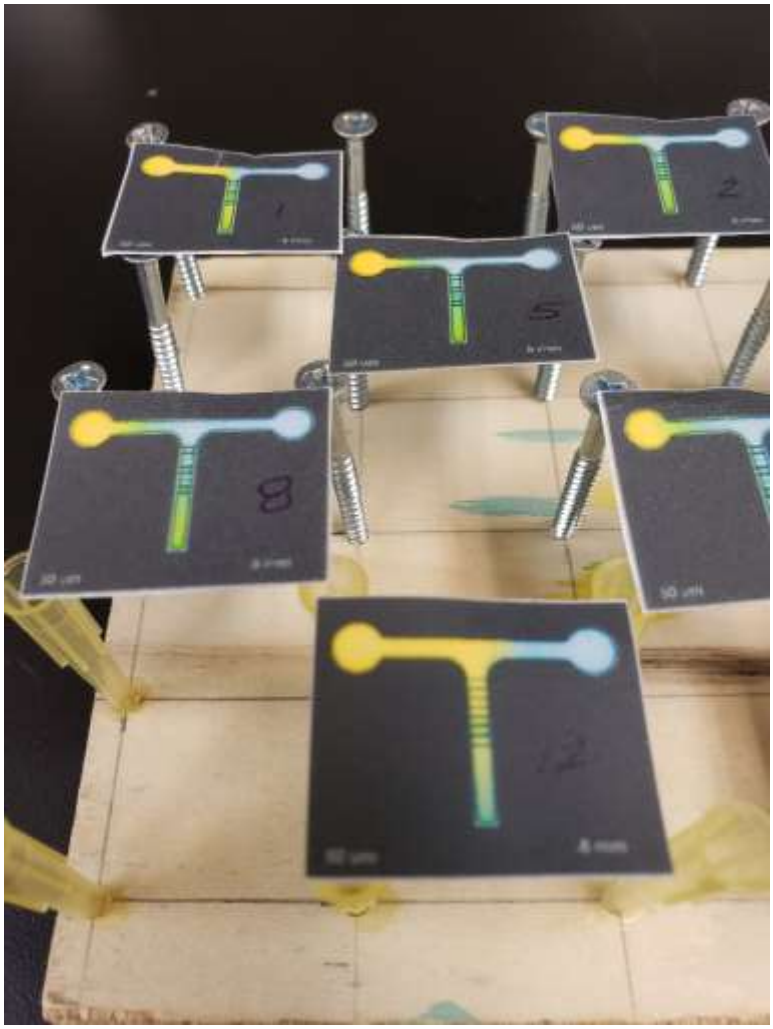

Figure 3-2: Image of the peg stand used to elevate the devices during device testing to allow the fluid to flow uninhibited through each device.

Fifteen microliters of each the yellow and blue fluid were placed on the on the devices, one after the other into the separate inlet reservoirs. The fluids were allowed to flow down into the mixing channel together. The devices were dried in air before they were digitally imaged.

3.2.3 Imaging

Once dry, the devices were numbered and imaged. The images were taken in a light-controlled box (Figure 3-3) with a Samsung Galaxy Note 9 rear facing camera. The

devices were placed in a 3D printed square as a way to align the devices for the picture. A ruler was also placed in the photos for scale. Images were transferred to a computer using OneDrive.

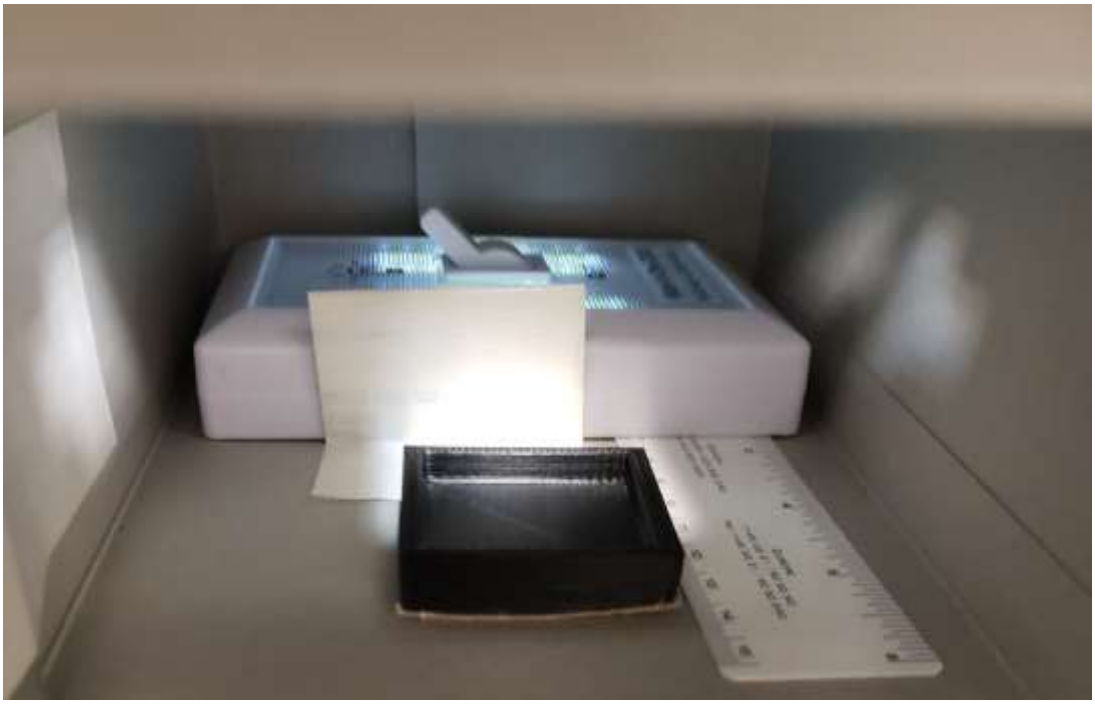

Figure 3-3: Image of the inside of the light controlled box with the 3D printed device holder and ruler for scale.

3.3 Image Analysis

3.3.1 MATLAB Code

A MATLAB code was written to determine the RGB color code of the designated area from the images of the devices. The code prompts the user to select the images to be analyzed. The first selected image is then be displayed on the screen and the user is prompted to move the pre-sized rectangle to the area that needs to be analyzed. The size of the rectangle was first determined by the user and the size was saved in the MATLAB workspace. The default user box size was 1 mm by 0.85 mm. The rectangle size is maintained for all preceding images and code runs, unless the workspace is cleared. In

this work, all analyses were done with the same size rectangle, as MATLAB was never closed and the workspace cleared. The area directly after the flow disrupting lines and the at the end of the channel were both analysis in this project. Figure 3-4 shows the areas that were analyzed on each device using the code.

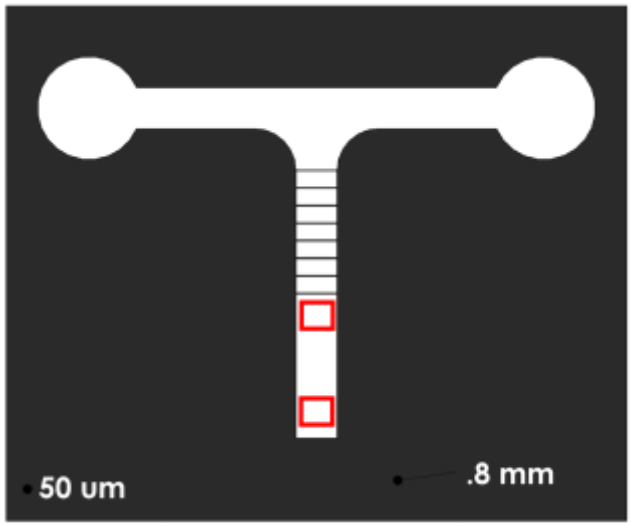

Figure 3-4: Device marked with the two user defined regions (red rectangles) that were analyzed on each device using the MATLAB code. The rectangle size used in the MATLAB code was 1 x 0.85 mm.

For the selected area in each image, the code will sum all of the red, green, and blue RGB numbers respectively and output an average RGB color code for the given area. The output of the code is an excel worksheet with each averaged RGB color code for every selected image analyzed.

3.3.2 RGB Analysis

The RGB color code for each device was imported into Excel, and Eq. 3-1was used to convert the three parameters to a singular number that emphasized the green parameter.

$$K_G = \frac{G}{R + G + B} \qquad \textbf{Eq. 3-1}$$

K_G was normalized by an idealized green value, which was determined by running 30 devices that had equal parts blue and yellow mixed in solution placed on the device and then allowed to dry. The green standard devices were then run through the MATLAB code, and the average K_G of the green devices (A_G) were used to normalized the test devices using Eq. 3-2.

$$N = \left|\frac{K_G}{A_G} - 1\right| \qquad \textbf{Eq. 3-2}$$

The N values closest to zero indicate a color that is closest to the ideal green standard.

After this analysis was done on a large number of devices, it was noticed the N values for some devices that were visually yellow were closer to zero than the N values for some devices that were visually green. To eliminate the influence of yellow in the analysis, the red value of RGB was removed from the analysis, making Eq. 3-3 the corrected analysis.

$$K_{GC} = \frac{G}{G + B} \qquad \textbf{Eq. 3-2}$$

This equation was applied to the green standards and the new average was used for the normalization. Figure 3-5 shows the RGB analysis and the GB analysis of a device with a test region that is visually yellow and a device with a test region that is visually green to show how the GB analysis limited that influence of yellow within the analysis.

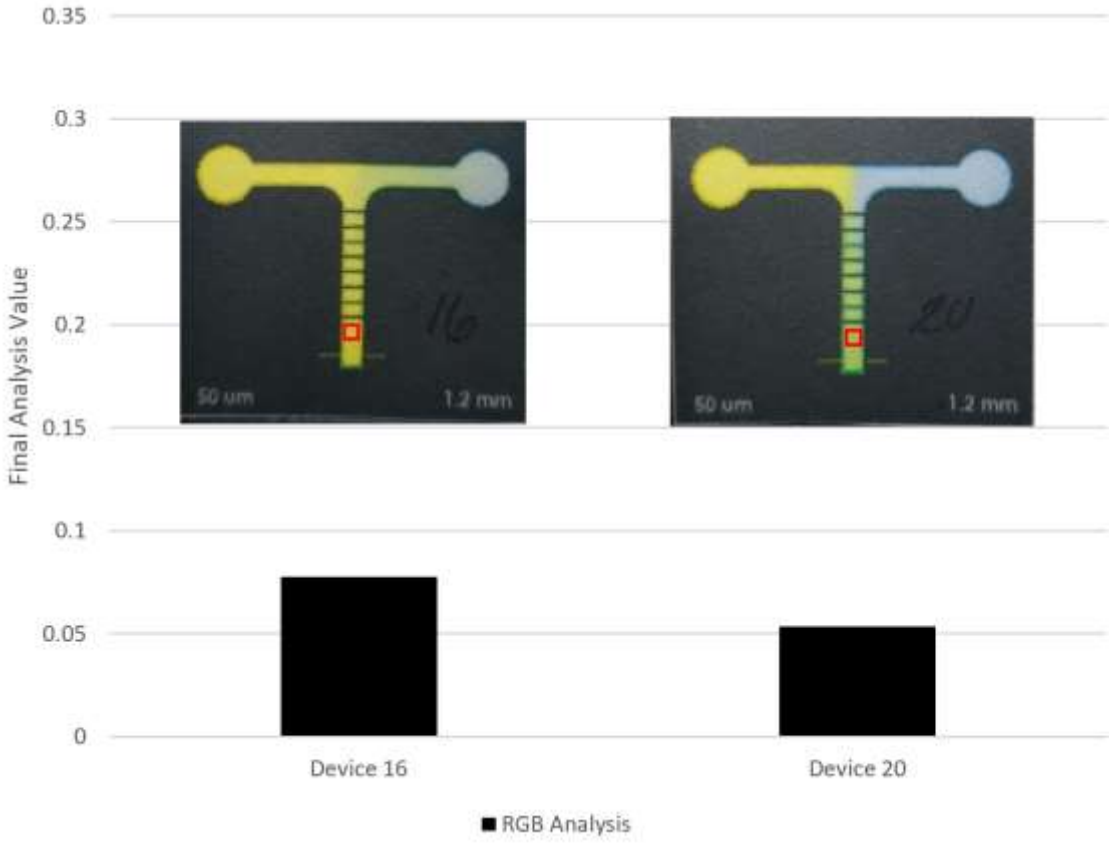

Figure 3-5: RGB analysis of a device with a test region that is qualitatively yellow and a device with a test region that is qualitatively green to show that the RGB analysis does not significantly distinguish the yellow regions from the green regions.

CHAPTER 4

DEVICE DESIGN

In this chapter, the preliminary results are analyzed and the parameters of the device designs are evaluated and validated in going from digital to the paper. The line width is the first parameter to be evaluated and is initially tested as isolated lines. The lines are then evaluated within the device, with steps taken to reduce the printed size of the lines. Once the line width was determined, the line spacing was evaluated and verified to its designed parameters. Finally, the inlet angle was measured on the printed devices to verify the parameters.

4.1 Preliminary Results

Preliminary testing was done to determine if adding flow-disrupting structures straight across the channel would improve the mixing of two different color fluids. The test was also performed to determine if the structures would block the fluid flow through the device. The flow disrupting line dimensions used were a designed line thickness of 50 μm and a line spacing of 1 mm. Figure 4-1 shows the preliminary results of a device with and without flow-disrupting structures.

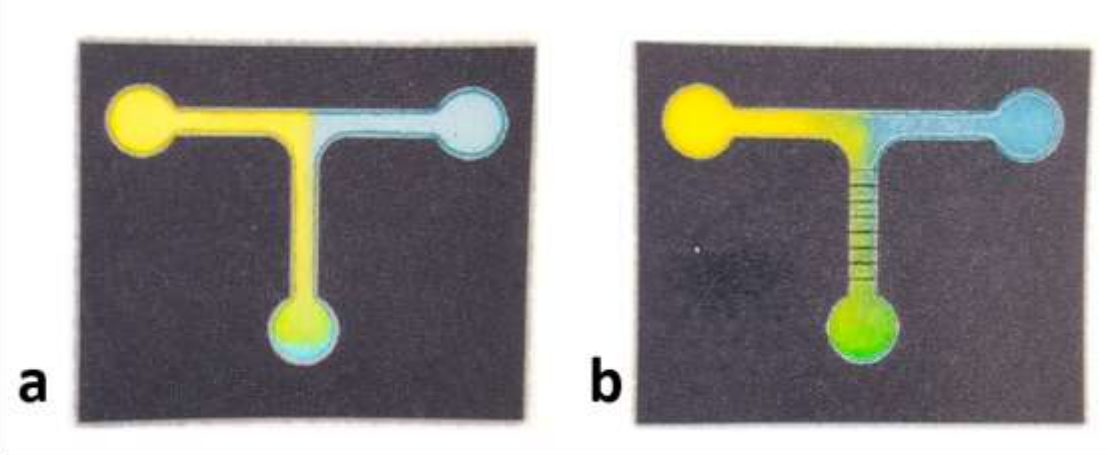

Figure 4-1: Side-by-side comparison of preliminary test results. Channel without the flow disrupting line design incorporated (A) and with the flow disrupting line design incorporated (B). (A) Shows negligible mixing within the end reservoir of the device where (B) shows increased mixing, but the mixing is not uniform in the reservoir.

Based on a visual analysis of the end reservoir, the device with no flow disrupting lines shows little mixing, and both starting colors can be seen in the end reservoir. For the device with the flow disrupting lines, green can be distinctly seen in the end reservoir but the lack of uniformity suggests optimization is possible in the design.

The penetrated wax depth of the flow disrupting lines into the paper is a critical aspect of this design. The width of the lines is thought to directly correlate to the depth of the wax after heating the wax in the oven. This idea was demonstrated by Carrilho et al. in 2009 in their paper on understanding wax printing [13]. Figure 4-2 shows how the initial width of the wax affects the spreading and depth of the wax after heating.

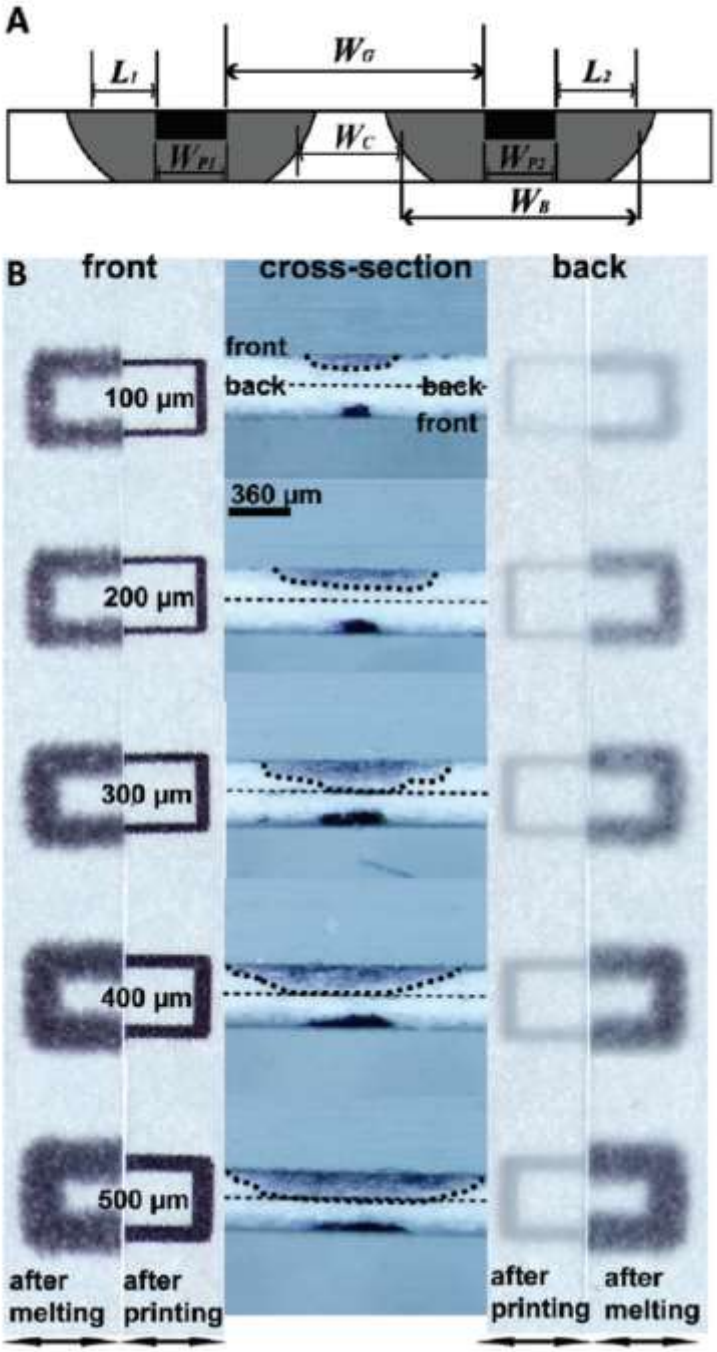

Figure 4-2: (A) Shows the schematic of the wax spreading and (B) shows the front, back, and cross-sectional images before and after melting the wax through the paper. The 100 µm and 200 µm line thicknesses in (B) do not completely penetrate the channel and thus would still allow fluid to flow. [13].

Carrilho et al. indicated that the line thickness needed to be less than 300 µm to allow fluid flow through the mixing channel. They also showed that we can regulate the depth of the wax by the width of the printed wax on the chromatography paper.

4.2 Flow Disrupting Line Width (α)

4.2.1 Dimension Validation

Before determining the optimal line width for the flow disrupting structures, the printed line width needed to be determined. It was suspected that the designed line widths were not being accurately printed on the paper, within the devices. Isolated lines were designed and printed at 200 µm, 150 µm, 100 µm, 50 µm, 40 µm, and 30 µm lines with 1 mm spacing. Figure 4-3 is a print out of the isolated lines that were measured with the laser scanning confocal microscope and the laser scanning microscope images of the 30 µm, 100 µm, and 200 µm.

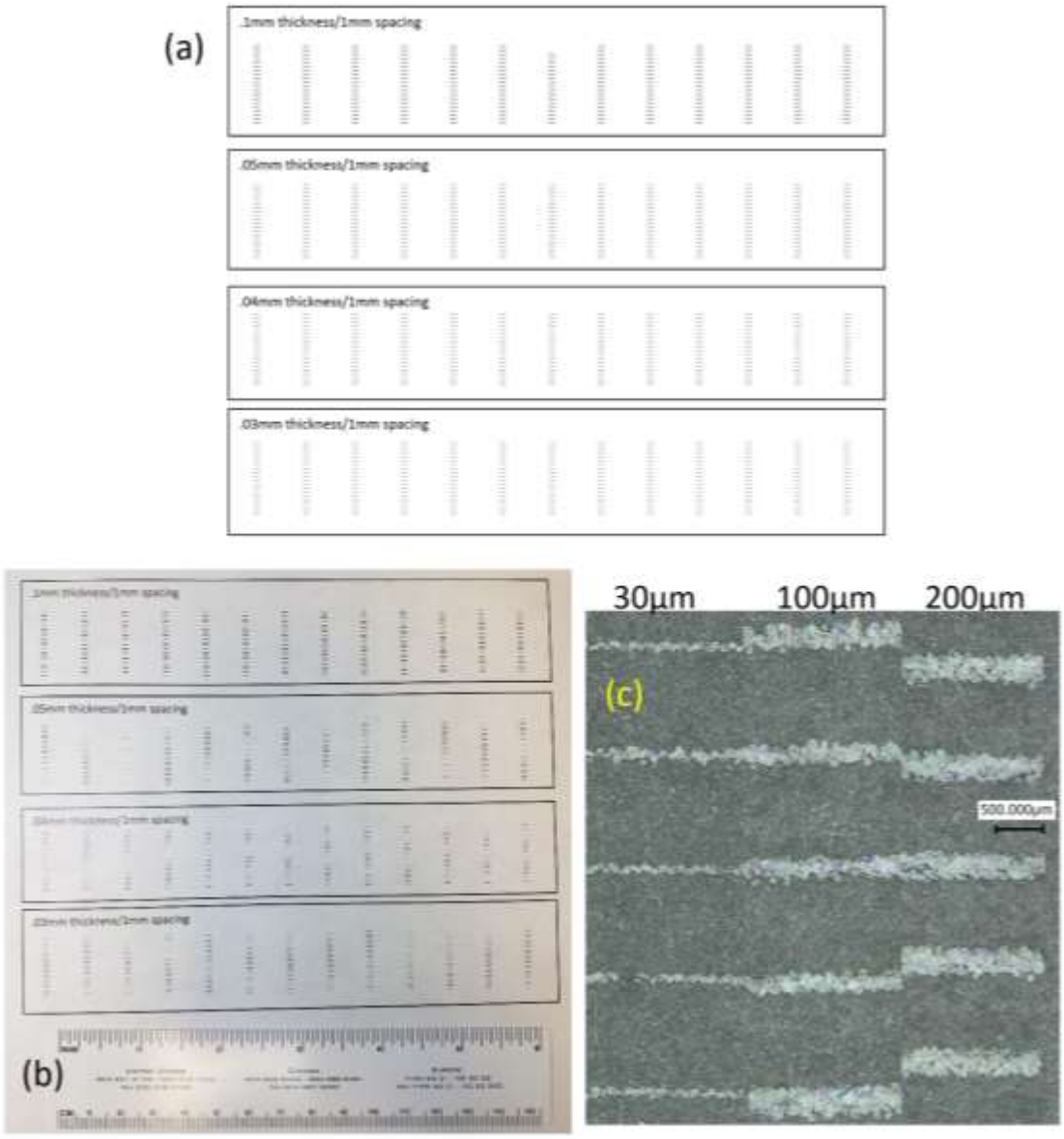

Figure 4-3: Isolated line in the Microsoft Word program before printing (A), the print out of the isolated lines (B), and the laser scanning confocal microscope images of the printed lines designed at 30 µm, 100 µm, and 200 µm (C).

Figure 4-3(B) shows that the printer duplicates small lines inconsistently, given that Figure 4-3(A) is the word document that was sent to the printer. Some lines were obviously larger than the rest in the column and some lines were missing from the planned design. The lines were measured using the laser scanning confocal microscope's

VK viewer software. Five lines were measured out of each column of lines. Figure 4-4 is the plot of the average measured line width of each of the designed line widths.

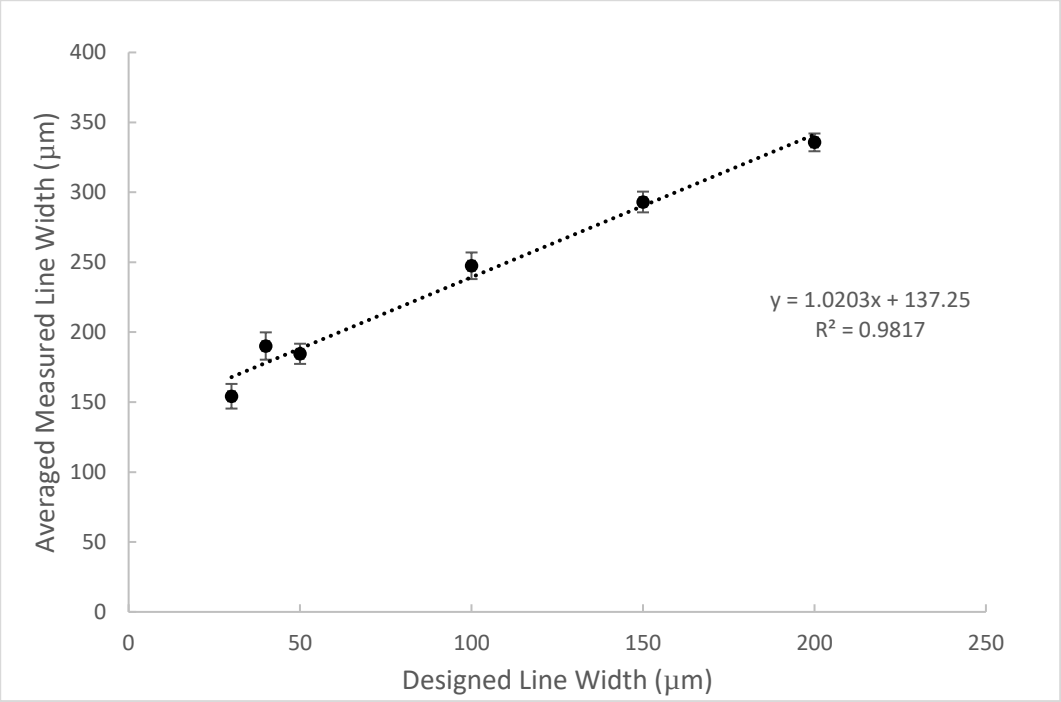

Figure 4-4: Plot of the average measured line width of the designed line width of the isolated lines with 95% confidence intervals, n = 65. There is a linear increase in the averages has the designed width increases, but the all measured widths are greater than their designed widths.

All measured lines were larger than the designed line widths; however, the measured line widths increased in a linear fashion with a slope near one. As the line width increased the difference between the designed width and the measured width decreased. Since the trend between the measured line widths was linear, it was thought that a scaling issue caused some of the discrepancies between the designed line width and the measured widths.

4.2.2 Cropping

When the device design images are saved from Solidworks, the background in Solidworks also gets saved as part of the image. To accurately size the devices back to their original design once they are inserted into Microsoft, the background needs to be cropped from the image. The differences between the designed line widths and the measured line widths was thought to be in part to the inconsistencies in the cropping within Microsoft Word. In an attempt to reduce these inconsistencies, the lines were measured in the devices and the devices were cropped in Adobe Photoshop. These devices were compared to the same device designs cropped in Microsoft Word.

In Word, the cropping has to be done manually by moving the cropping tool to all four edges of the device. This process leaves room for error in the cropping, and subsequently the sizing of the device. In Adobe Photoshop, the magic wand tool was used to select the white background around the device and then cut it from the image, leaving only the device design. The devices were then saved again and imported into Microsoft Word where they were resized to the designed size. Figure 4-5 is the average measured line width of the Photoshop-cropped devices compared to the measured line width of the devices cropped in Microsoft Word.

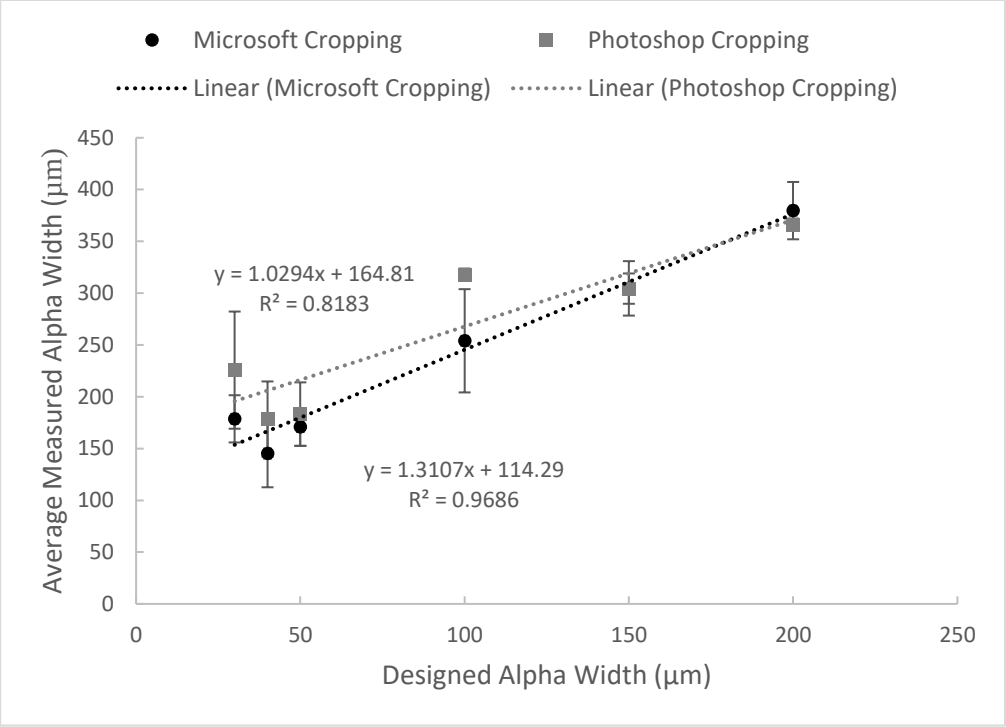

Figure 4-5: Plot of the average line width measurements in the devices cropped using the Microsoft Word cropping feature and the Photoshopped cropping feature with standard deviation bars, n=5. Shows little difference and overlapping standard deviation bars between the devices that were cropped in Photoshop versus in Word.

The averages of the photoshopped devices were greater than the Microsoft cropped devices for the smaller width devices from 30 µm to 100 µm. The photoshop process did not improve the line width results of the devices (and in some cases, increased variability to the dimensions of the final printed products), and we returned to the original process of using Microsoft Word for image cropping.

4.2.3 In Device Measuring

Line widths for the wax printing on the devices were measured with the laser scanning confocal microscope at 40, 50, 80, 100, 150, and 200 µm (Figure 4-6). The 30 µm line width was deemed too inconsistent and was on average greater than the line widths for both the designed widths of 40 µm and 50 µm.

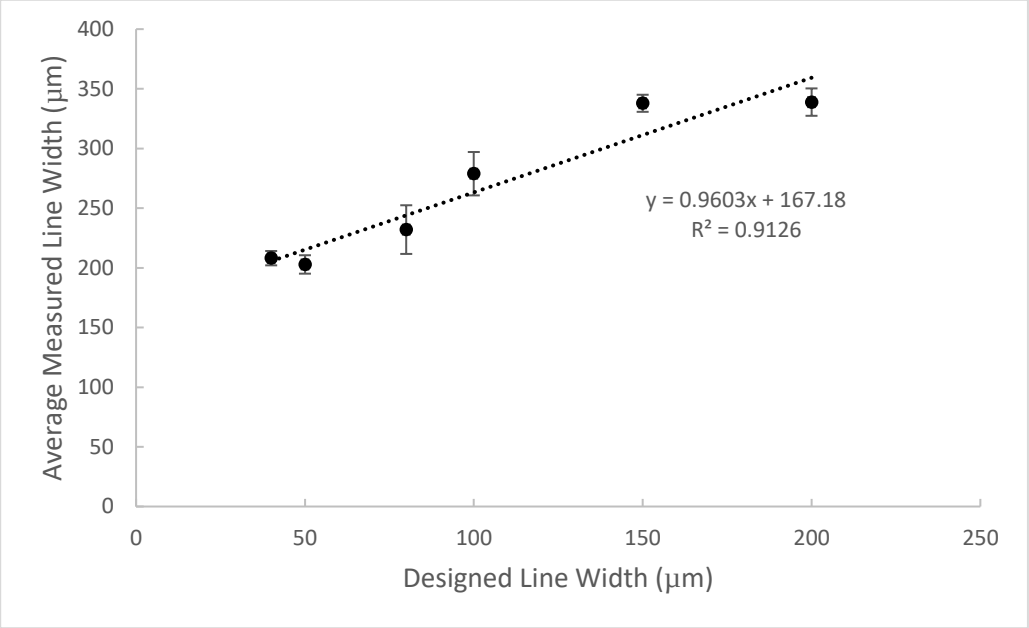

Figure 4-6: Plot of the average measured line width for wax printed on the devices, with 95% confidence intervals, n = 50. On-device width was linear with the designed width, but the measured lines were still larger than the designed widths.

The conclusion from these results is that it is impossible for the printer to print the dimensions of the line widths that were originally designed in Solidworks. It was also determined from these measurements that the smallest dot size the printer could print was 60 µm. Therefore, all subsequent device line widths will not match the widths designed in the computer. A flow test (Figure 4-7) was performed in which 12 µL of each color was loaded into an inlet reservoir and allowed to flow to the mixing channel. The test verified that all the designed line widths above 50 µm (wax-printed as 202 µm) blocked the fluid flow through the channel. Thus, these widths were no longer considered as usable in the mixing channel.

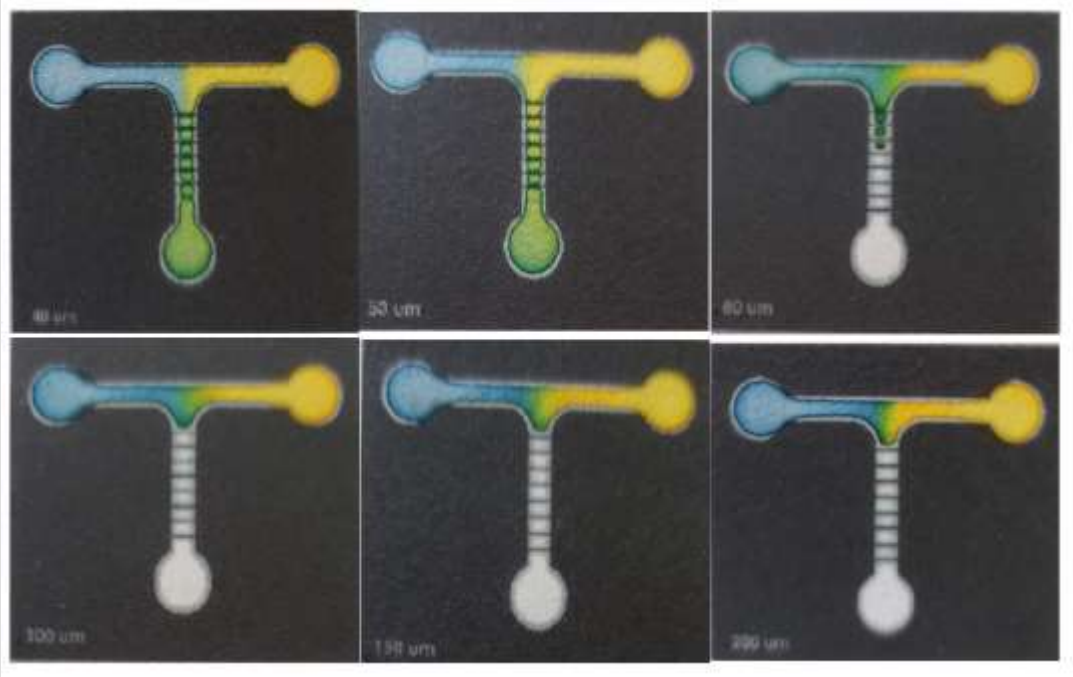

Figure 4-7: Flow test for devices with line widths of 40 µm, 50 µm, 80 µm, 100 µm, 150 µm, and 200 µm.

4.2.4 JPEG vs TIF

In one final effort to reduce the measured line width of the printed devices and increase the resolution, the devices were saved as TIFs and the measured line widths were compared to the previously printed JPEG devices. Figure 4-8 shows the line width measurements of the JPEG saved devices and the TIF saved devices for designed widths of 40 µm, 50 µm, and 80 µm.

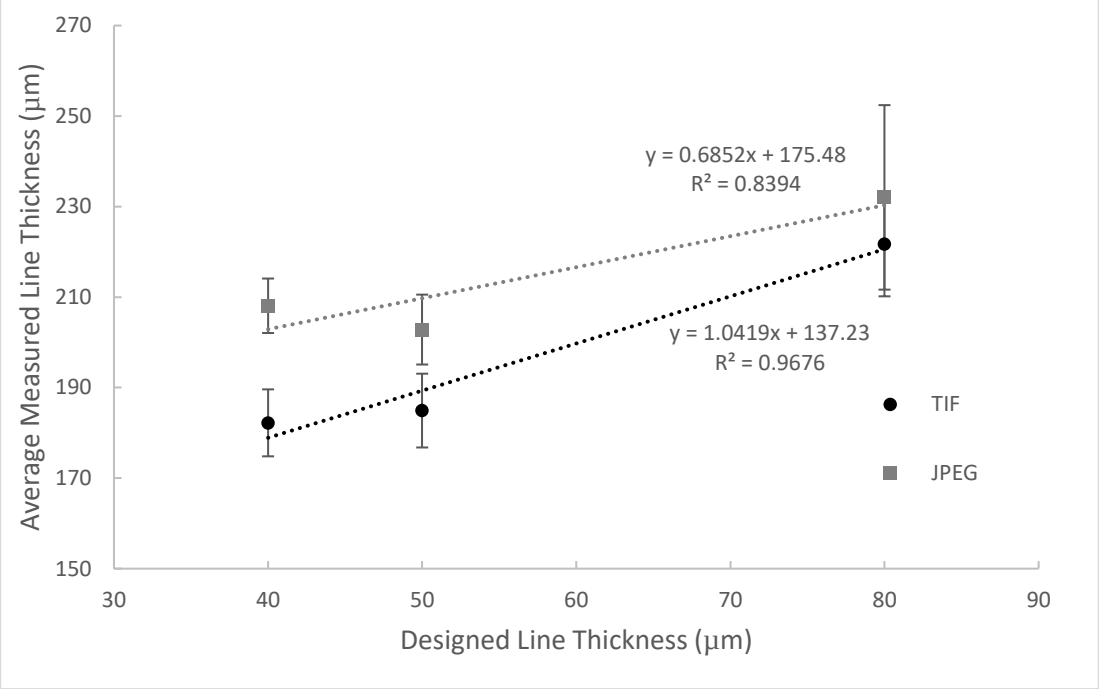

Figure 4-8: Plot of the average measured line width JPEG and TIF printed devices with 95% confidence intervals, n=50. Shows the linearity of both the JPEG and TIF devices and that the measured lines of the TIF devices are smaller in average width and therefore closer to the target line widths that the JPEG devices.

The TIF devices averaged measured lines were all less than the average measured widths of the JPEG devices. A two-tailed t-test of unequaled variance was conducted for each the 40 µm, 50 µm, and 80 µm to compare whether the differences between the TIF and JPEG were statistically significant. The 40 µm and 50 µm p-value were both less than 0.05, indicating that they are statistically different. The 80 µm had a p-value of greater than 0.05, but after a flow test was conducted on the TIF devices, it was found that the designed 80 µm lines still blocked the mixing channel from fluid flow. From these results, it has been concluded that the TIFs provided a greater resolution and thus more accurate line widths once the devices were printed and that TIFs will be used for all

remaining experiments. Table 4-1 shows the average measured line width and the calculated percent error.

Table 4-1: Table of the designed line widths and the corresponding measured line widths within the printed TIF devices with the calculated percent error.

Designed Line Width	Averaged Measured Line Width	Percent Error
40 µm	182 µm	355%
50 µm	185 µm	270%
80 µm	221 µm	176%

4.3 Flow Disrupting Line Spacing (β)

The next parameter to be evaluated was the spacing (β) of the flow disrupting lines within the mixing channel. The spacing measurements that were evaluated were 0.5, 0.8, 1, and 1.2 mm. It was determined that anything below 0.5 mm would block the channel due to the proximity of the lines and the wax spreading caused by the heating process in the oven. It was also determined that anything above 1.2 mm spacing would require an elongation of the channel in order to keep the number of flow disrupting lines consistent. Consistency of the channel length is needed keep the mixing channel length as small as possible. Figure 4-9 shows devices with designed 50 µm line widths and 0.5, 0.8, 1, and 1.2 mm spacing.

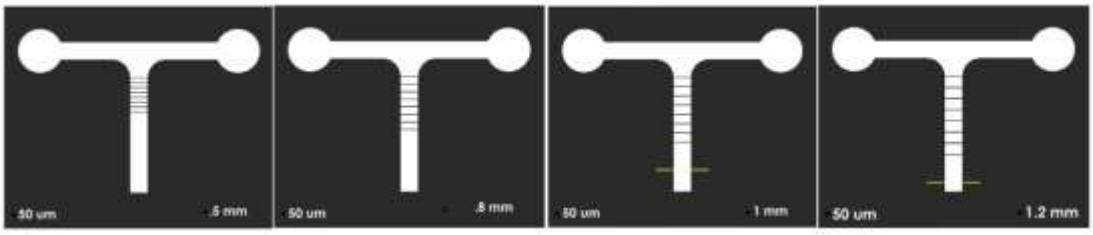

Figure 4-9: Mixing devices with designed 50 µm line widths and 0.5, 0.8, 1, and 1.2 mm spacing.

4.3.1 Validation Measuring

Before conducting the mixing efficiency test, the designed spacing was measured in ImageJ to validate the dimensions of the designs. Figure 4-10 shows the measured spacing against the design spacing at 0.5, 0.8, 1, and 1.2 mm before and after heating the devices in the oven.

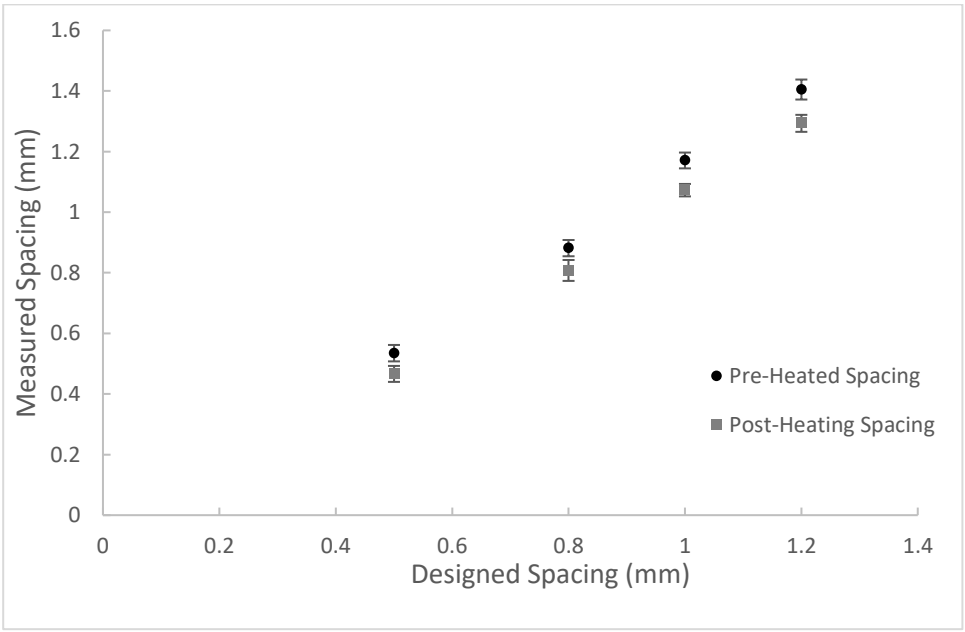

Figure 4-10: Average measured line spacing at 0.5, 0.8, 1, and 1.2 mm before and after heating the devices in the oven with 95% confidence intervals, n = 70. Shows the preheating spacing is slightly greater that the designed spacing but the post heating spacing is closer to the designed.

Before heating the devices to penetrate the wax through the paper, the average spacing measurement was larger than what was designed for each device. After heating the devices, the spacing between the lines shrank due to the wax spreading, this shrinkage was beneficial because the post-heating spacing measurements were closer to the designed spacing widths. After device testing (explained in more detail in Chapter 5), we deemed 0.5 mm line spacing to be the optimal line spacing for mixing on-chip with these flow disrupting structures.

4.4 Inlet Angle (γ)

Once the ideal flow disrupting line parameters of α and β were determined, the next parameter to be evaluated was the inlet channel angle (γ). The inlet angles evaluated were 0°, 15°, 30°, 45°, and 60°. Figure 4-11 shows the mixing devices with designed with50 µm line widths and 0.5 mm spacing and the inlet angles to be tested.

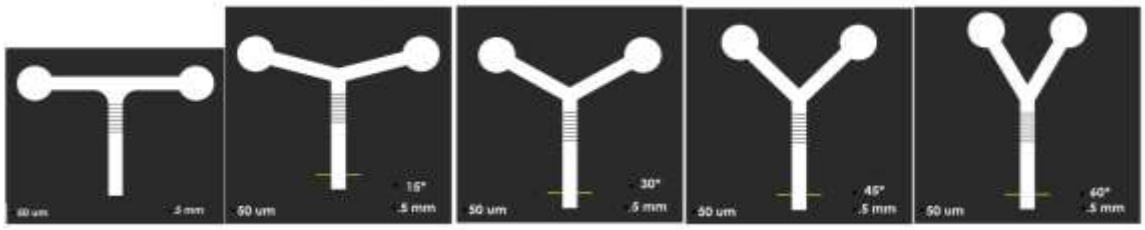

Figure 4-11: Mixing devices with designed 50 µm line widths and 0.5 mm spacing and inlet angles of 0°, 15°, 30°, 45°, and 60°.

4.4.1 Validation Measuring

The inlet angles were measured using ImageJ to verify the designed inlet angles on the printed devices. Figure 4-12 shows the results of measuring the devices as compared to their designed angles.

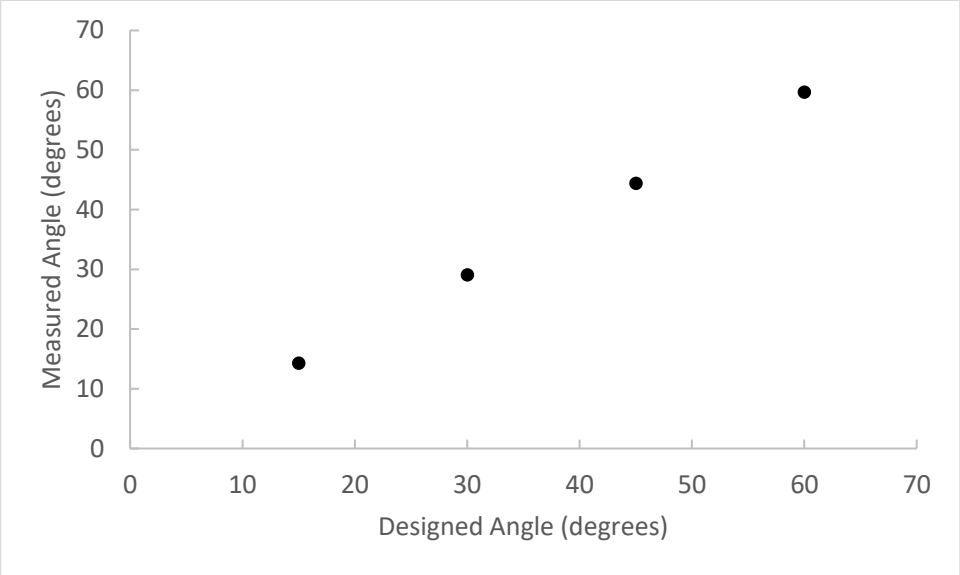

Figure 4-12: Measured inlet angles of 15°, 30°, 45°, and 60° with 95% confidence interval bars (too small to see), n=30. Shows the measured inlet angles are consistent with the designed inlet angles.

The measured angles of the printed devices were consistent and the average of each set was within less than 1° of the designed angles.

CHAPTER 5

DEVICE TESTING

In this chapter, the RGB and GB analysis is further discussed and the decision to use the GB analysis is further validated. The chapter then describes the mixing efficiency test used to determine the optimal line width for mixing. Then the mixing efficiency tests are run to determine the optimal line spacing of the devices and whether the mixing is greater directly after the flow disrupting structures or at the end of the channel. The inlet angle mixing efficiency test are then evaluated along with the best mixing location on the devices. Finally, the devices are compared to devices with no flow disrupting structures at the various inlet angles tested.

5.1 RGB and GB Analysis

Initially, the analysis performed on the average RGB color code for each device was done by dividing the green value by the addition of the red, green, and blue values, $\left(\frac{G}{R+G+B}\right)$, and then by normalizing the results by the ideal green color that went through the same analysis. The lower the normalization value, the closer the area was to the ideal green color. While preforming this analysis and normalization on a number of devices, it was noted that many devices that displayed no mixing and were qualitatively yellow had a normalization value lower than many devices that had some mixing and appeared

qualitatively green. It was decided to remove the red value of the RGB color code from all the analysis to remove the influence of the yellow in the samples. The two analyses were then compared by analyzing to same sample. The sample was created by placing equal amounts of yellow and blue fluid solutions on a square of chromatography and allowing the fluids to flow together to form green in the middle. The RGB color code was determined across the square in a line using ImageJ, followed by analysis, normalization, and plotting in Excel. Figure 5-1 compares the two analyses as the line on the sample went from yellow to green to blue.

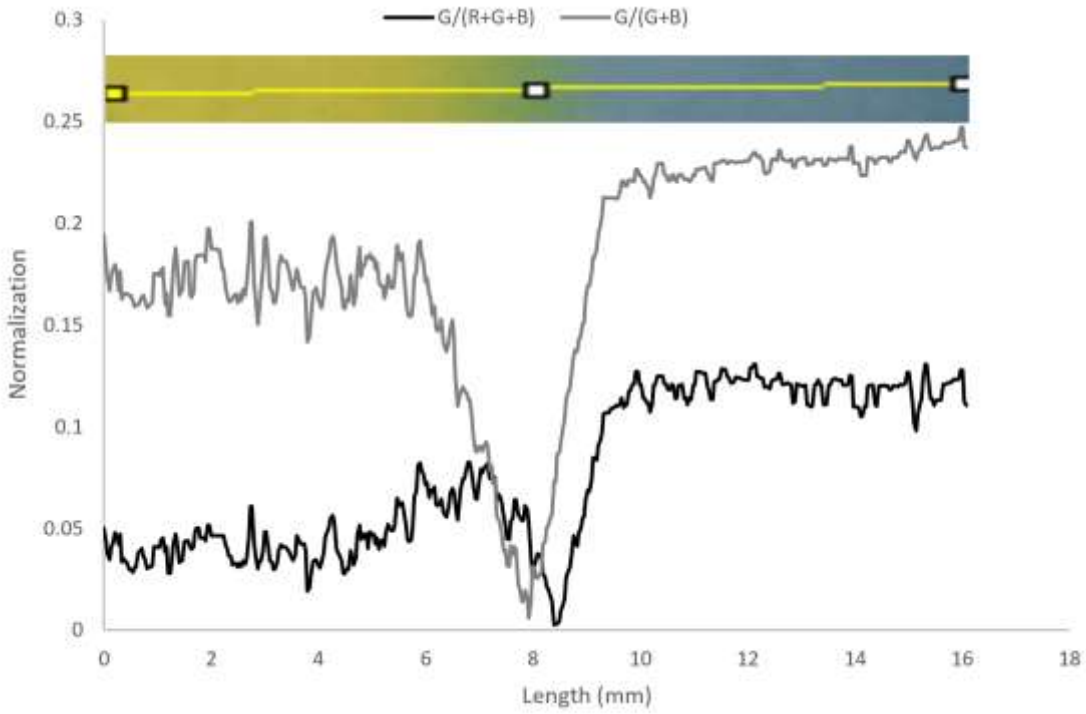

Figure 5-1: Comparison of the results of the $\frac{G}{R+G+B}$ (K_G) normalization analysis and the $\frac{G}{G+B}$ (K_{GC}) normalization analysis as the test line goes from yellow, to green, to blue. The GB analysis created a greater distinction from the yellow and blue to the target green than the RGB analysis.

This shows that the $\frac{G}{G+B}$ analysis creates a greater distance from zero for the straight yellow and blue colors than the $\frac{G}{R+G+B}$ analysis. The downward peak, corresponding to the most ideal green color of the sample, is better aligned with the visually green section of the sample. The $\frac{G}{G+B}$ analysis was then used to analyze all previous and remaining devices. Upon re-analysis of the previous devices, the devices that were visibly yellow had a higher normalization value than with the $\frac{G}{R+G+B}$ analysis, and the visibly green devices were lower. Figure 5-2 shows the RGB analysis and the GB analysis of a device with a test region that is visibly yellow and a device with a test region that is visibly green to show how the GB analysis limited that influence of yellow within the analysis.

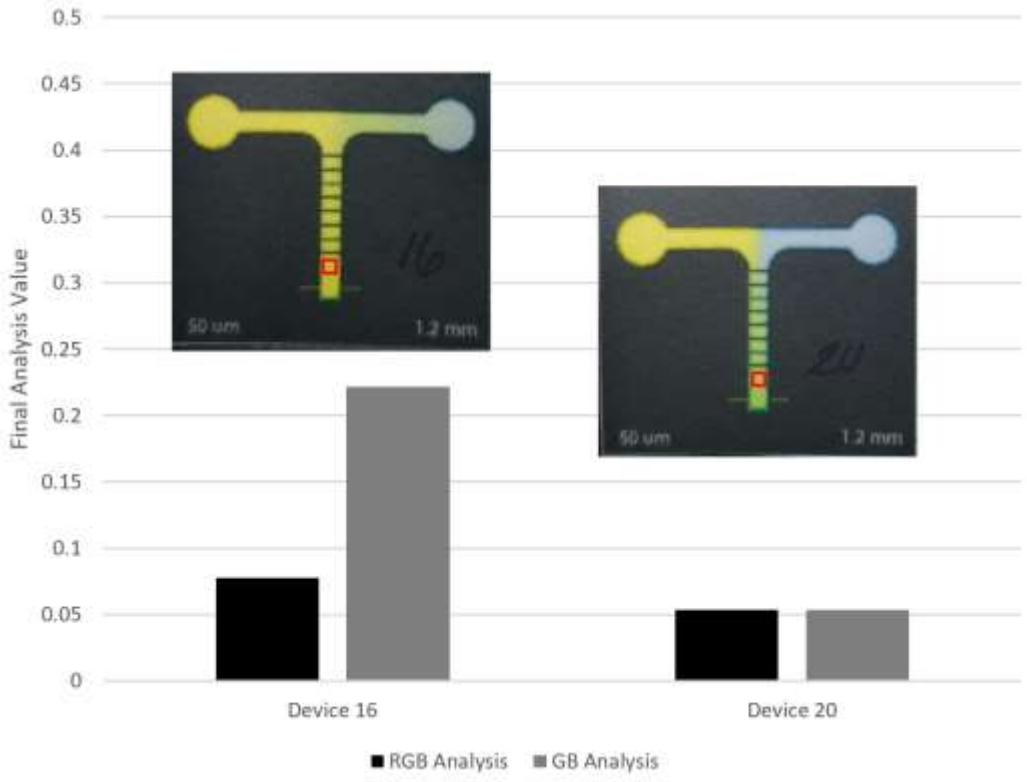

Figure 5-2: RGB analysis and the GB analysis of a device with a test region that is visibly yellow and a device with a test region that is visibly green to show how the GB analysis limited that influence of yellow within the analysis.

5.2 Line Width (α) Mixing

5.2.1 Alpha Line Width Mixing Efficiency Test

Since all the line widths above the designed 50 µm blocked the fluid flow through the channel, only 40 µm and 50 µm designed line widths were tested for mixing efficiency. Figure 5-3 shows the mixing efficiency test comparing 40 µm and 50 µm line widths measured at the end of the channel and after the flow disrupting lines. The standards for blue, yellow, and green, analyzed with the same method as the test devices, are also shown for comparison.

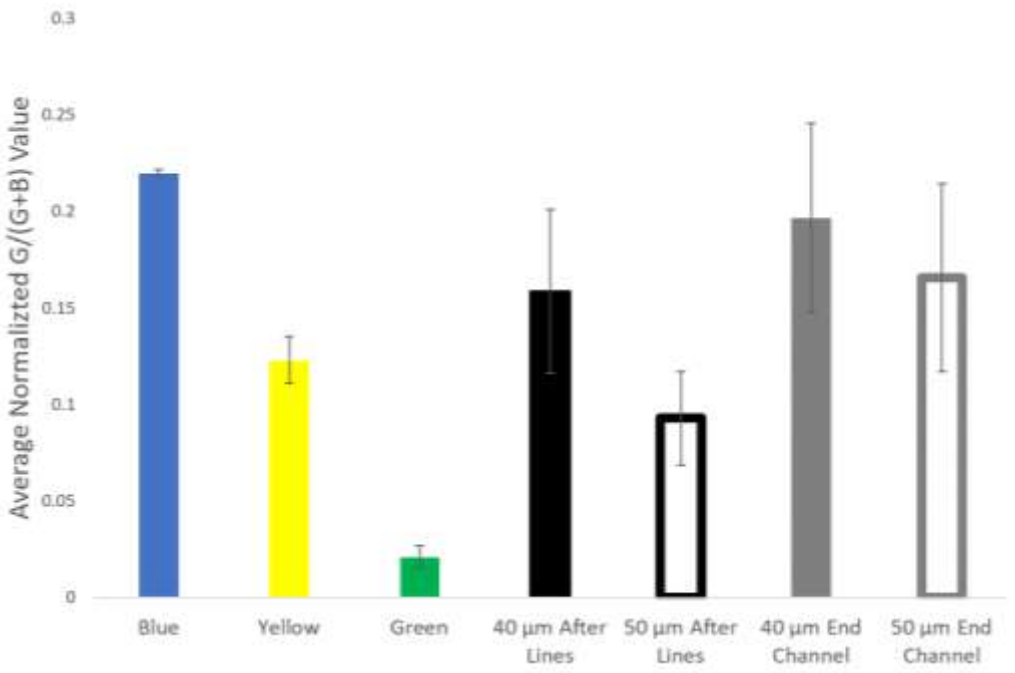

Figure 5-3: Average normalization value of the test devices for 40 µm and 50 µm line widths at the end of the channel and after the flow disrupting lines with the standards for blue, yellow, and green. The data have 95% confidence interval bars with n = 30. The directly after lines analysis are closer to the target than the end channel analysis and the 50 µm analyses are closer to the target than the 40 µm analyses.

From these results and a two-tailed unequal variance t-test which gave a p-value of greater than 0.05, it was determined that the mixing efficiency between 40 and 50 µm

designed line widths were not significantly different from each other for the end channel measurements. The after the flow disrupting lines measure were both closer to the target green than the end channel measurements. A two-tailed unequal variance t-test for the after flow disrupting lines of 40 µm and 50 µm came back with a significant p-value of 0.0069 with the designed 50 µm being closer to the target green than the devices at 40 µm. The designed 50 µm is considered the optimal α value for the physical constraints of the wax printer and of the wax spreading within the paper.

The end channel normalization values were farther from zero than the values directly after the lines. These larger values could be caused by the chromatography paper, which is designed to separate and filter fluidic samples. A test was done to determine the effects the chromatography paper has on mixed solutions. The yellow and blue dyes were mixed in solution and then 15 µL of the mixture was placed in the inlet reservoir of a 75 mm long channel and allowed to diffuse along the channel. After the channels dried, they were imaged. Figure 5-4 show three of the devices run in this test.

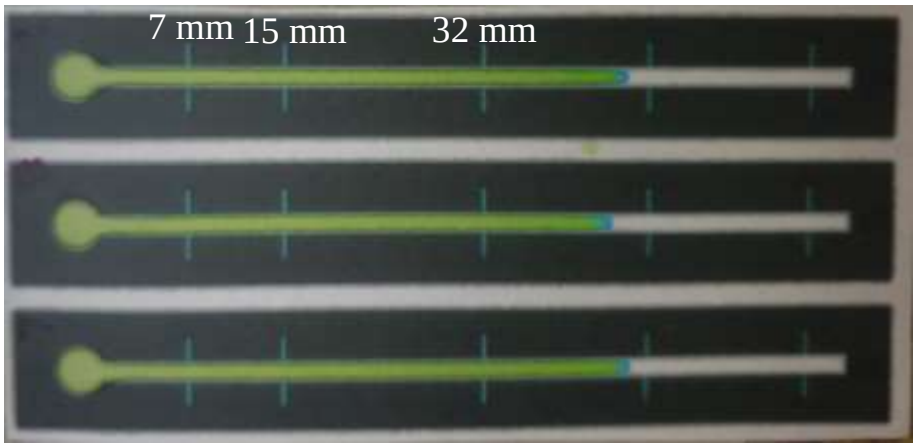

Figure 5-4: Three of the devices run in the chromatography flow test. The results show that the blue dye diffuses ahead of the rest of the mixture.

The device shows that the solution remains together until the end, where some of the blue continues by its self. The molecular weights of the food coloring dyes used are published as $534.4\,\frac{g}{mol}$ for the yellow dye and $445.4\,\frac{g}{mol}$ for the blue dye [50]. The smaller molecular weight for the blue dye explains the leading diffusion of the blue dye observed in Figure 5-4. Figure 5-5 shows the average normalization analysis done in the inlet reservoir and at 7 mm, 15 mm, and 32 mm down the channel.

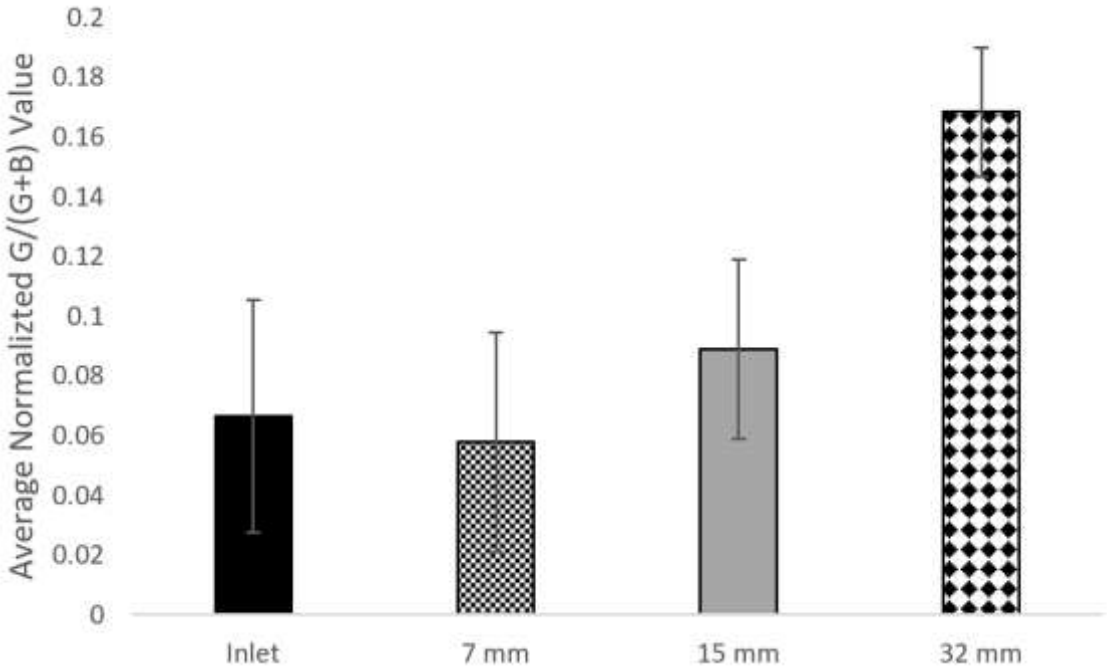

Figure 5-5: Shows the average normalization analysis done in the inlet reservoir and at 7 mm, 15 mm, and 32 mm down the channel. Each data set has a 95% confidence interval bar with n = 30. The data shows an increasing trend from 7 mm to 32 mm, meaning the dyes begin to separate as they flow down the channel.

Figure 5-5 shows that the average normalized GB value increases as the distance increases, excluding the inlet. The average at the inlet is greater than the average 7 mm down the channel, but a two-tailed t-test of unequal variance did not show significance, with a p-value of 0.740. The t-test run against the inlet and 15 mm and the against 7 mm

and 15 mm were also insignificant with p-values of 0.36 and 0.18, respectively. All t-test run against 32 mm were significant with p-values of 2.648×10^{-5} with the inlet, 2.94×10^{-6} with 7 mm, and 5.18×10^{-5} with 15 mm. This test shows that after the fluid flows out of the flow disrupting lines that the chromatography paper begins to separate the fluids, but that the fluid separation by the end of the device channel (15 mm) is not significant.

5.3 Line Spacing (β) Mixing

5.3.1 Mixing Efficiency Tests

With the line width optimized, the spacing between the flow disrupting lines were adjusted to determine the optimal spacing for mixing efficiency. Spacing values of 0.5, 0.8, 1, and 1.2 mm were evaluated. The mixing efficiency evaluations were run at both the end of the mixing channel and directly after the flow disrupting lines. Figure 5-6 shows the mixing efficiency test for the flow disrupting line spacing taken at the end of the channel and directly after the flow disrupting lines.

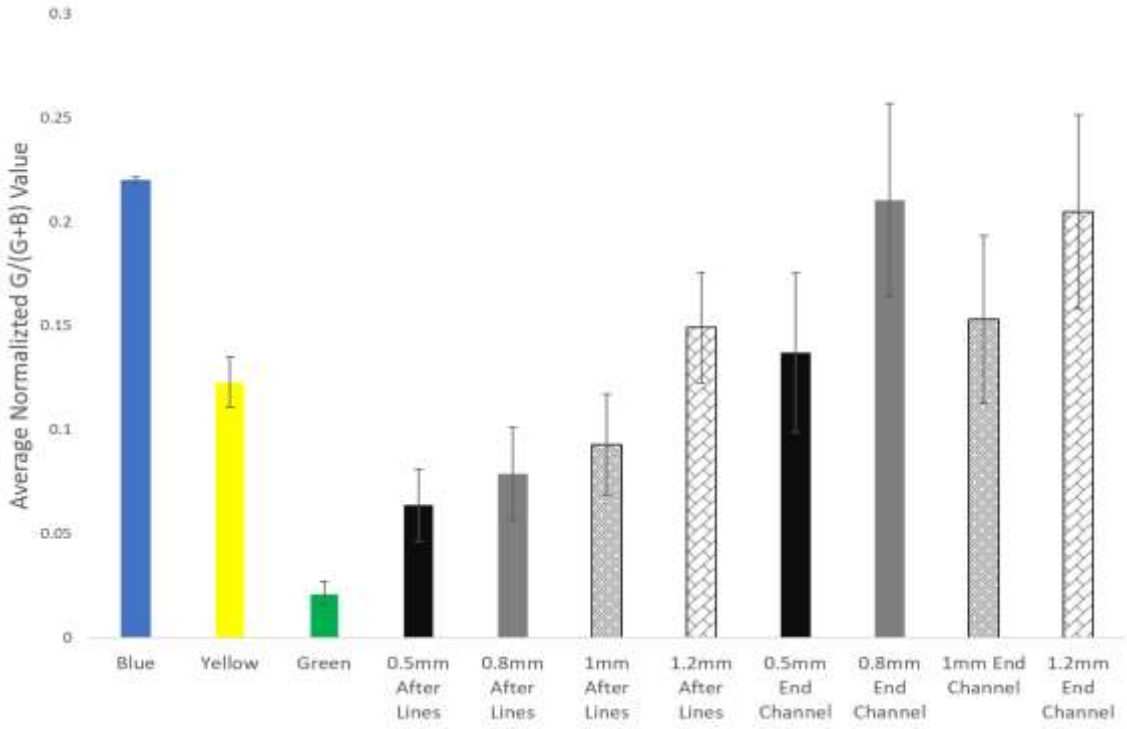

Figure 5-6: The average mixing efficiency of the devices with line spacing of 0.5 mm, 0.8 mm, 1 mm, and 1.2 mm at the end of the channel and after the flow disrupting lines with the blue, yellow, and green standards for comparison. Each data set has a 95% confidence interval bar with n = 30. Again, the after lines analyses are closer to the target than the end channel analysis and for both the 0.5 mm analysis is the best.

For all of the spacing widths tested, the GB values at the end of the channel are farther from zero than those immediately distal to the flow disrupting lines. Two-tailed unequal variance t-tests were run between each spacing size at the end of the channel analysis and immediately distal to the flow disrupting lines. Each test was significant with the p-values of 2.34×10^{-5} for 0.5 mm, 8.89×10^{-8} for 0.8 mm, 0.0075 for 1 mm, and 0.007 for 1.2 mm. For both the end channel and immediately distal measurements, the 0.5 mm spacing was the closest to zero, and the standard green, in both their respective groups. From the results, the 0.5 mm spacing is considered the optimal spacing

with the 50 μm flow disrupting line widths. The best mixing from these parameters is directly after the flow disrupting structures.

5.4 Inlet Angle (γ) Mixing

The inlet angle (γ) was evaluated next. The angles evaluated were 0°, 15°, 30°, 45°, and 60°. The device also had flow disrupting lines with an $\alpha = 50$ μm and $\beta = 0.5$ mm. The mixing efficiency for each device was calculated using the MATLAB code and Excel. Figure 5-7 shows the mixing efficiency results of the different inlet angles.

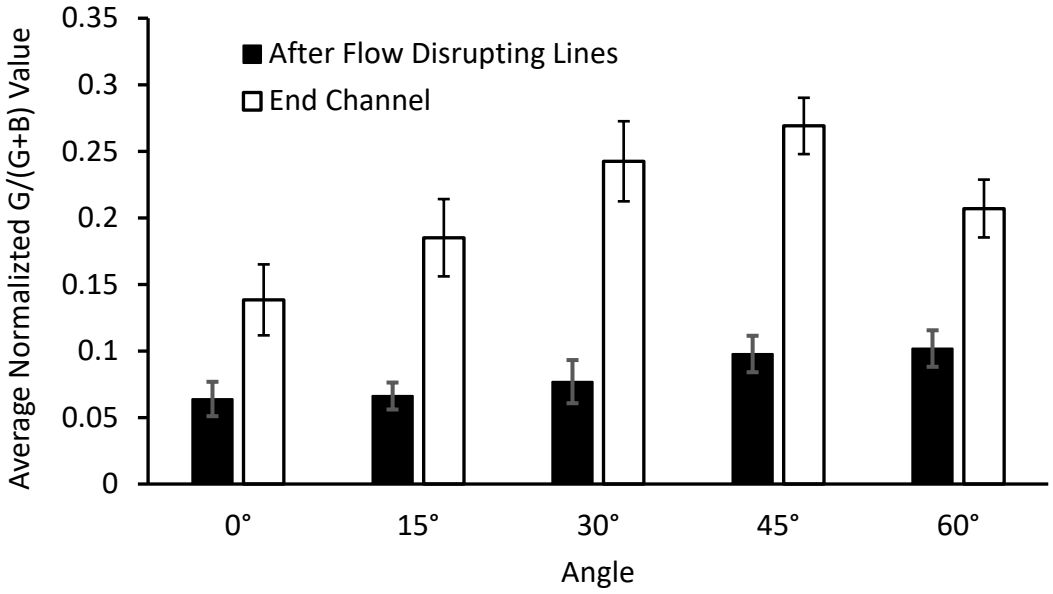

Figure 5-7: Mixing efficiency results for the devices with designed 50 μm line widths and 0.5 mm spacing and inlet angles of 0°, 15°, 30°, 45°, and 60°. Measurements were taken after the flow disrupting lines and at the end of the channels. 95% confidence interval bars, n=30. All after lines measurements are closer to the target than the end channel measurement with the inlet angle of 15° being the closest.

Again, the end channel measurements were farther from the target green than the measurements taken directly after the flow disrupting lines. For the measurements taken directly after the flow disrupting lines, the 15° inlet angle with the flow disrupting lines

had the smallest average and thus the closest to the target green. However, when the two-tail unequal variance t-test were run comparing 15° and the other inlet angles, none were significant except the t-test comparing the 15° inlet to the 60° inlet. The only other significant t-tests were 0° vs. 45° and 0° vs. 60° with p-values of 0.033 and 0.023 respectively. Overall, the increased inlet angle in conjunction of the flow disrupting structures did not lower the average GB values of the devices with $\alpha = 50$ μm and $\beta = 0.5$ mm and the greater angles of 45° and 60° actually increased the average value of the GB analysis, indicating less effective mixing.

5.5 No Mixing Structures Comparison

To validate the above results, the GB analysis was done on devices with no flow disrupting lines with the different inlet angles. The analysis was done at the end of the channel and immediately distal to the flow disrupting lines which is 7 mm from the inlet junction. Figure 5-8 shows the results from the inlet angle analysis above with the devices with $\alpha = 50$ μm and $\beta = 0.5$ mm and compares them to the devices with no flow disrupting lines.

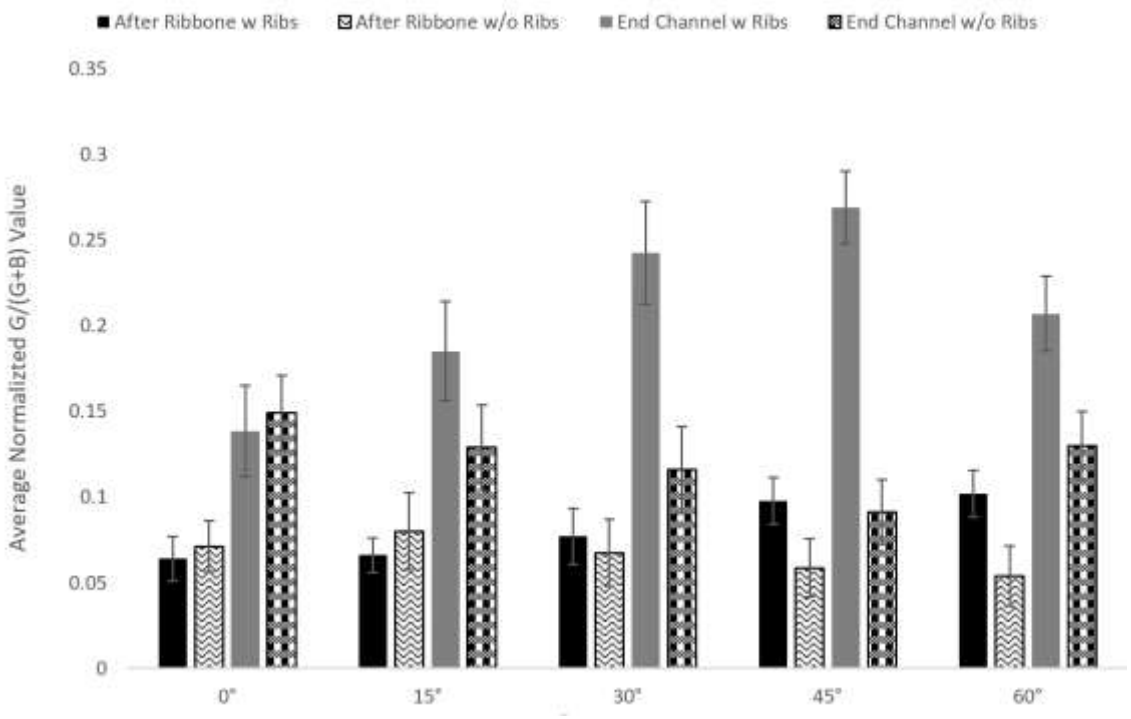

Figure 5-8: Average mixing efficiency results for the devices with designed 50 µm line widths and 0.5 mm spacing and devices with no flow disrupting lines with inlet angles of 0°, 15°, 30°, 45°, and 60°. Measurements were taken after the flow disrupting lines and at the end of the channels. 95% confidence interval bars, n=30. All after lines measurements are closer to the target green than the end channel measurements. For the lower inlet angles, the devices with flow disrupting lines are closer to the target but the higher the inlet angle the better the mixing is in the devices with no flow disrupting lines than the ones with.

As expected, the measurements taken at the end of the channel were farther from the target green than the analysis done 7 mm from the inlet junction. What was not expected was that for both the end channel and the 7 mm analyses, the devices with no flow disrupting lines were closer to the target green than the devices with the flow disrupting lines for inlet angles of 30° and above. Two-tailed unequal variance t-test were run for each inlet angle for the devices with the flow disrupting structures against the devices with no flow disrupting structures for the measurements taken 7 mm from the inlet junction (after the flow disrupting structures). The t-test run for the 0°, the 15°, and

the 30° inlet angle were not significant with p-vales of 0.519, 0.340, and 0.496, respectively. The t-test run for the inlet angles of 45° and 60° were significant with p-values of 0.014 and 0.0049, so for the analyses done “after the flow disrupting lines” or 7 mm after the inlet junction, the mixing efficiency is the best for the inlet angles of 45° and 60° with no flow disrupting lines. For the inlet angles 0°, 15°, and 30°, the mixing efficiency is slightly improved by the flow disrupting lines, but not significantly from no flow disrupting lines.

CHAPTER 6

CONCLUSIONS AND FUTURE WORK

6.1 Conclusions

This work has successfully improved the mixing in paper-based microfluidic devices with the incorporation of flow disrupting structures and with the adjustment of the angle of the inlet channels. Mixing was improved with flow disrupting lines with a designed thickness (α) of 50 µm, which correlates to an actual width of ~185 µm, and a spacing width (β) of 0.5 mm. Mixing was also improved when the inlet angle was adjusted to 45° and 60° with no flow disrupting lines. The mixing was more efficient with inlet angles of 45° and 60° with no flow disrupting lines than with flow disrupting lines with the same inlet angle. The mixing efficiency is also the best directly after the flow disrupting structures or for the inlet angled devices with no flow disrupting lines, 7 mm from the inlet junction.

The biggest limitation of this project is the substrate used to create the devices: the chromatography paper. By design, chromatography paper is designed to separate and filter fluids, which is the opposite of what this project is trying to achieve. This design is most likely why the end channel analysis was farther from the target green. As the fluid moved farther down the channel with no flow disrupting structures, the dyes would begin to separate.

The next big limitation of this project was the physical limitations of the wax printer. The printer works by depositing drops of mixed wax onto the paper. The size of these drops was around 60 µm in diameter. The printer does not deposit these drops in a straight line and instead deposits them in a diagonal pattern, shown in Figure 6-1. This pattern created a minimum line width thickness of ~100 µm. The printer also could not print a set of lines consistently and with a width variety of sizes.

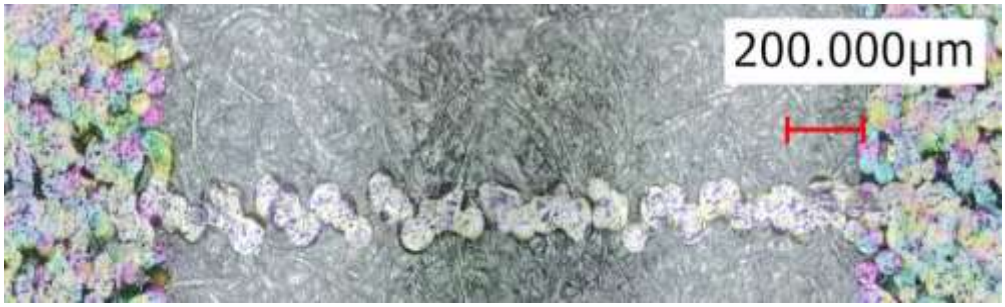

Figure 6-1: Laser Scanning confocal microscope image of a wax printed line in a paper-based microfluidic device.

Another limitation is the ability to successfully quantify the mixing efficiency of two colors. Although mixing was quantified with great accuracy and success, relying on the mixture of only two colors to determine mixing efficiency is not ideal. The results of these experiments would benefit greatly from use of a different analytical technique to quantify mixing, such as an assay that requires mixing to bind a higher quantity of molecules. In addition to this consideration, for greater quantitative consistency, the user defined rectangles used in the MATLAB program for the test region needs to be a fixed size in the code, as opposed to being set on demand by the user. While on-demand setting allows greater program flexibility, it introduces a layer of variability when the program is used for the same analysis, as in this study, where experiments analyzed at different time

periods could be analyzed with differing sized boxes, producing the possibility for higher intra-experimental variability.

6.2 Future Work

6.2.1 Greater Wax Penetration Control

For this project, the depth of the wax through the paper for the flow disrupting lines was solely based on the width of the printed wax for the lines. Greater control of the depth of the penetrated wax would allow for more accurately defined devices with varying depths to aid in mixing. This capability would also increase the range of line widths that can be tested in the future. A potential result would be to increase the width of the flow disrupting lines while limiting the depth of penetration through the paper, thus keeping the channel free from blockage.

One possible method uses double-sided printing. This technique deposits wax on both sides of the paper. When the paper is heated the wax flows from both the top and the bottom and meets in the middle. The flow channels could be printed with this technique, while the flow disrupting lines are printed on only one side of the paper. Thus, the flow channels penetrate the paper fully while the disrupting lines penetrate only partially, preventing obstruction of the channels.

Another potential method to increase the flow disrupting line width while not blocking the channel is to use another color wax. Throughout the test, only the color black was used to create these devices. The default way for the wax printer to print black using the wax is to print with black wax and a mixture of the magenta, cyan, and yellow waxes. Figure 6-2 shows the laser scanning confocal microscope image of one of the wax printed devices before wax penetration. The many wax droplets that make of the device

are a combination of the magenta, cyan and yellow wax. On the macro scale however, the wax appears to be black. Thus, when the printer uses this color combination to print in black, it uses more wax than it would if black wax alone were used. If the flow disrupting lines were set to be a single color, they would require the use of one color and deposit less wax on the paper.

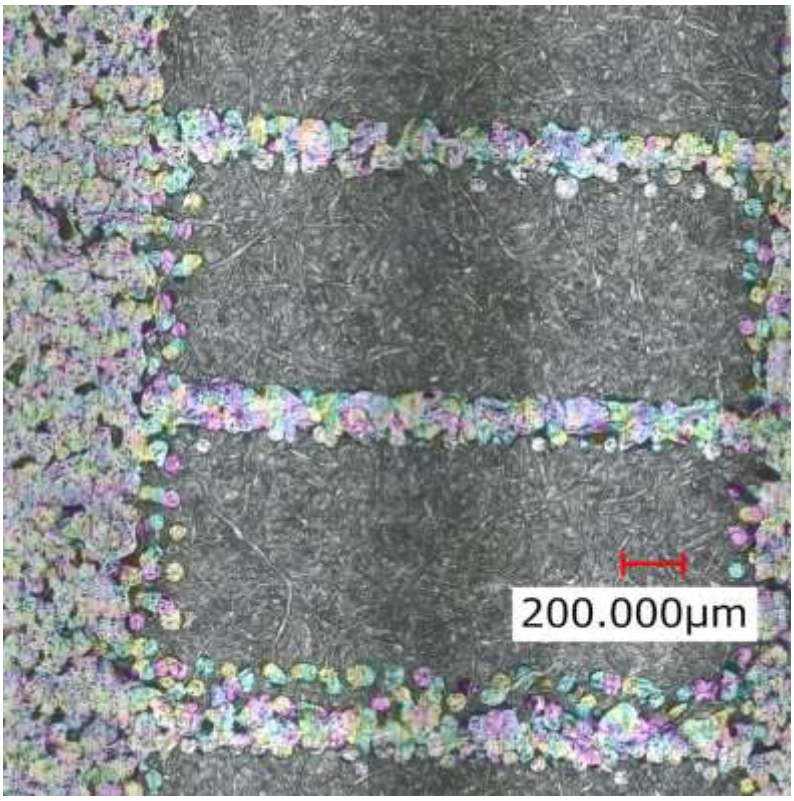

Figure 6-2: Laser Scanning confocal microscope image of a wax printed paper-based microfluidic device.

6.2.2 Test with Protein-Antibody Assay

To further validate the improved mixing capabilities of the devices with the flow disrupting structures, a protein-antibody assay can be developed and run through the devices. Results from this assay would be compared to those from devices with no flow disrupting structures. If the flow disrupting structures increase mixing within the channel,

the concentration of bounded protein-antibody compounds will be greater in the devices with the flow disrupting structures than the devices without.

6.2.3 ELISA Testing

Once the increased mixing of these devices is proven within a protein-antibody assay, development of an effective paper-based microfluidic ELISA can begin. The 96-well plate ELISA requires hours of incubation time to allow the molecule interactions to take place, which is driven by diffusion. The paper-based device with the flow disrupting structure could create an ideal environment to speed up the molecular interactions required for the ELISA test.

APPENDIX A

MATLAB CODE AND OUTPUT

A.1 MATLAB Code

```
%G2RGB_Ratio_Identifier
%Developed by Kevin Holly

%Select folder and identify the files

% defaultdir = uigetdir('C:\');
[filenames, folder] =
uigetfile([pwd,filesep,'*.*'],'MultiSelect','on','*.*');

%preallocate
G2RB_Ratio_index = zeros(1,length(filenames));

%First loop!!!
i=1;
Post_image = imread([folder,filenames{i}]);

figure
imshow(Post_image)

uiwait(msgbox('Please select the region that you would like
to get green/(red+blue) percentage','ROI Selection'))

% getrect()
% drawrectangle

if exist('coord','var') == 1
    lol=gca;
    h=imrect(lol,coord);
    %add click button
    uiwait(msgbox(["Please move the rectangular box to the
correct position";"Then click 'Ok' to continue"],"I don't
care"))
    coord = getPosition(h);
else
    h=imrect();
    coord = getPosition(h);
end

mask = createMask(h);
figure
imshow(mask)

blank = zeros(size(mask));

%Create color mask
Color_mask(:,:,1) = mask;
Color_mask(:,:,2) = mask;
Color_mask(:,:,3) = mask;

%
Red_mask = zeros(size(Color_mask));
```

```
Red_mask(:,:,1) = mask;
%
Green_mask = zeros(size(Color_mask));
Green_mask(:,:,2) = mask;
%
Blue_mask = zeros(size(Color_mask));
Blue_mask(:,:,3) = mask;

pixelcount = sum(sum(mask));
ROI_image = Color_mask.*double(Post_image);
Red_image = Red_mask.*double(Post_image);
Green_image = Green_mask.*double(Post_image);
Blue_image = Blue_mask.*double(Post_image);

imshow(uint8(ROI_image))
imshow(uint8(Red_image))
imshow(uint8(Green_image))
imshow(uint8(Blue_image))

Sum_Red_pixelvalues = sum(sum(sum(Red_image)));
Sum_Green_pixelvalues = sum(sum(sum(Green_image)));
Sum_Blue_pixelvalues = sum(sum(sum(Blue_image)));

Mean_Red = Sum_Red_pixelvalues/pixelcount;
Mean_Green = Sum_Green_pixelvalues/pixelcount;
Mean_Blue = Sum_Blue_pixelvalues/pixelcount;

% Percentage of G/RB

G2RB_Ratio_index(i) =
100*(Mean_Green/(Mean_Red+Mean_Green+Mean_Blue));

disp(['file ' num2str(i) ' completed!'])
close all

%For loop through each file
for i = 2:length(filenames)
Post_image = imread([folder,filenames{i}]);

figure
imshow(Post_image)

lol=gca;
h = imrect(lol,coord);

uiwait(msgbox('Please reposition the rectangular box before
selecting "ok" ','ROI Selection'));
%set(m, 'position', [100 440]);

% coord = getPosition(h);
mask = createMask(h);
figure
imshow(mask)
```

```
blank = zeros(size(mask));
%Create color mask
Color_mask(:,:,1) = mask;
Color_mask(:,:,2) = mask;
Color_mask(:,:,3) = mask;
%
Red_mask = zeros(size(Color_mask));
Red_mask(:,:,1) = mask;
%
Green_mask = zeros(size(Color_mask));
Green_mask(:,:,2) = mask;
%
Blue_mask = zeros(size(Color_mask));
Blue_mask(:,:,3) = mask;

pixelcount = sum(sum(mask));
ROI_image = Color_mask.*double(Post_image);
Red_image = Red_mask.*double(Post_image);
Green_image = Green_mask.*double(Post_image);
Blue_image = Blue_mask.*double(Post_image);

imshow(uint8(ROI_image))
imshow(uint8(Red_image))
imshow(uint8(Green_image))
imshow(uint8(Blue_image))
Sum_Red_pixelvalues = sum(sum(sum(Red_image)));
Sum_Green_pixelvalues = sum(sum(sum(Green_image)));
Sum_Blue_pixelvalues = sum(sum(sum(Blue_image)));

Mean_Red(i) = Sum_Red_pixelvalues/pixelcount;
Mean_Green(i) = Sum_Green_pixelvalues/pixelcount;
Mean_Blue(i) = Sum_Blue_pixelvalues/pixelcount;
% Percentage of G/RGB
G2RB_Ratio_index(i) =
100*(Mean_Green(i)/(Mean_Green(i)+Mean_Blue(i)));
disp(['file ' num2str(i) ' completed!'])
close all
end
%Save in Excel Sheet
f = '40alpha.xlsx';
headers = {'Filename','GB Ratio','Red Value','Green
Value','Blue Value'};
xlswrite([folder f],headers,1,'B1:F1')
xlswrite([folder f],filenames',1,'B2')
```

```
xlswrite([folder f],G2RB_Ratio_index',1,'C2')
xlswrite([folder f],Mean_Red',1,'D2')
xlswrite([folder f],Mean_Green',1,'E2')
xlswrite([folder f],Mean_Blue',1,'F2')
```

A.2 Output of the MATLAB Code

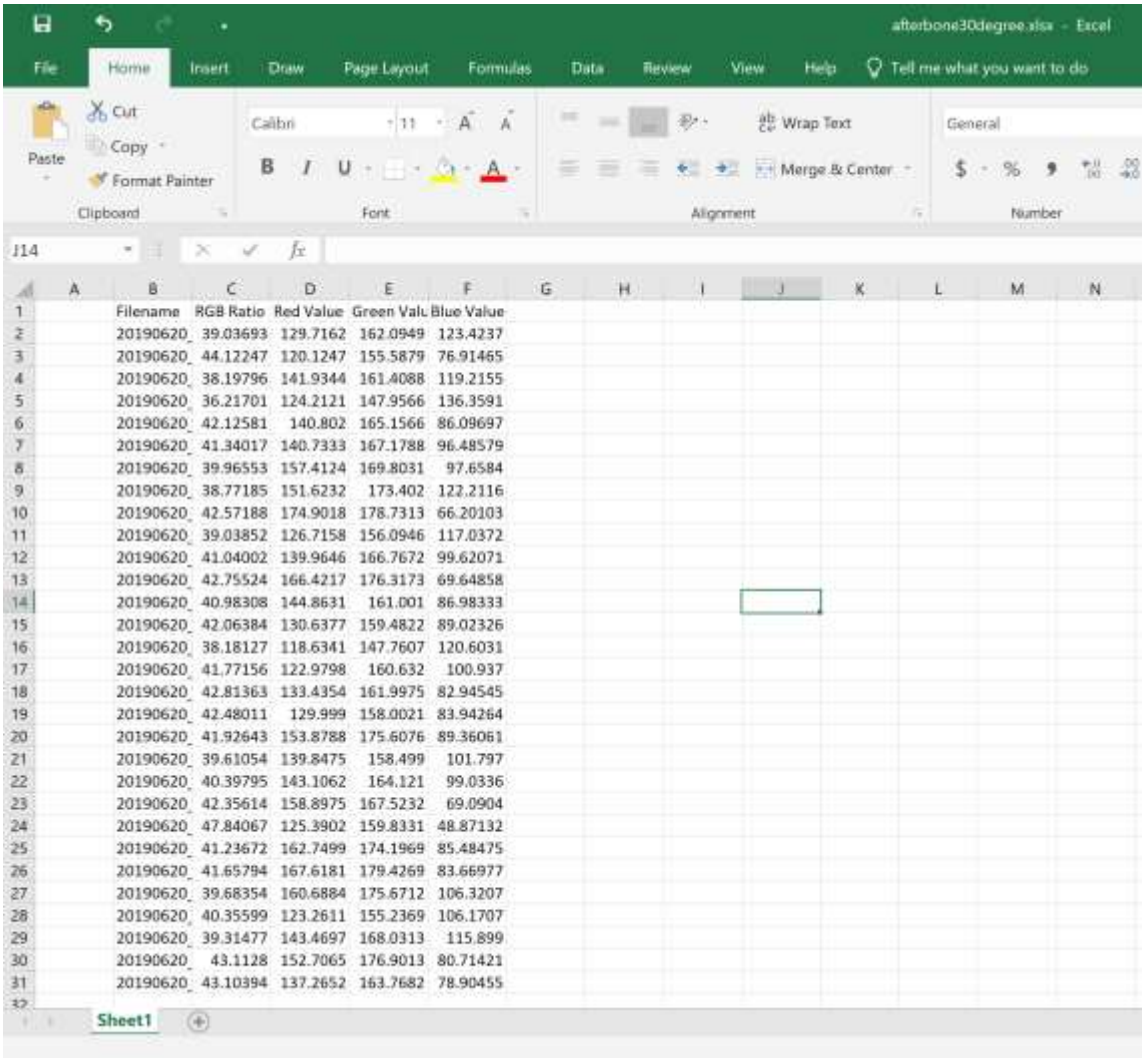

	Filename	RGB Ratio	Red Value	Green Valu	Blue Value
2	20190620_	39.03693	129.7162	162.0949	123.4237
3	20190620_	44.12247	120.1247	155.5879	76.91465
4	20190620_	38.19796	141.9344	161.4088	119.2155
5	20190620_	36.21701	124.2121	147.9566	136.3591
6	20190620_	42.12581	140.802	165.1566	86.09697
7	20190620_	41.34017	140.7333	167.1788	96.48579
8	20190620_	39.96553	157.4124	169.8031	97.6584
9	20190620_	38.77185	151.6232	173.402	122.2116
10	20190620_	42.57188	174.9018	178.7313	66.20103
11	20190620_	39.03852	126.7158	156.0946	117.0372
12	20190620_	41.04002	139.9646	166.7672	99.62071
13	20190620_	42.75524	166.4217	176.3173	69.64858
14	20190620_	40.98308	144.8631	161.001	86.98333
15	20190620_	42.06384	130.6377	159.4822	89.02326
16	20190620_	38.18127	118.6341	147.7607	120.6031
17	20190620_	41.77156	122.9798	160.632	100.937
18	20190620_	42.81363	133.4354	161.9975	82.94545
19	20190620_	42.48011	129.999	158.0021	83.94264
20	20190620_	41.92643	153.8788	175.6076	89.36061
21	20190620_	39.61054	139.8475	158.499	101.797
22	20190620_	40.39795	143.1062	164.121	99.0336
23	20190620_	42.35614	158.8975	167.5232	69.0904
24	20190620_	47.84067	125.3902	159.8331	48.87132
25	20190620_	41.23672	162.7499	174.1969	85.48475
26	20190620_	41.65794	167.6181	179.4269	83.66977
27	20190620_	39.68354	160.6884	175.6712	106.3207
28	20190620_	40.35599	123.2611	155.2369	106.1707
29	20190620_	39.31477	143.4697	168.0313	115.899
30	20190620_	43.1128	152.7065	176.9013	80.71421
31	20190620_	43.10394	137.2652	163.7682	78.90455

BIBLIOGRAPHY

[1] Thermofisher, "Overview of ELISA," [Online]. Available: https://www.thermofisher.com/us/en/home/life-science/protein-biology/protein-biology-learning-center/protein-biology-resource-library/pierce-protein-methods/overview-elisa.html. [Accessed 07 2019].

[2] X. Tan, M. K. K. Oo, Y. Gong, Y. Li, H.Zhu and X. Fan, "Glass Capillary based microfluidic ELISA for rapid diagnostics," *Analyst, vol.* 142, no. 13, pp. 2378-2385, 2017.

[3] Elveflow, "Microfluidics and Microfluidic Devices: A review," [Online]. Available: https://www.elveflow.com/microfluidic-tutorials/microfluidic-reviews-and-tutorials/microfluidics-and-microfluidic-device-a-review/. [Accessed 2019].

[4] C. Lee and L. Fu, "Recent Avances and Applications of Micromixers," Sensors and Actuators B: Chemical, vol. 259, pp. 677-705, 2018.

[5] E. C. Sweet, R. R. Mehta and R. Lin, "FINGER-POWRED, 3D PRINTED MICROFLUIDIC PUMPS," in 19th International Conference on Solid-State Sensors, Actuators *and Microsystems*, Kaohsiung, Taiwan, 2017.

[6] G. S. Fiorini and D. T. Chiu, "Disposable Microfluidic Devices: Fabrication, Function, and Application," Biotechniques, vol. 38, no. 3, *2018.*

[7] X. Wang, H. Jiang, Y. Chen, X. Qiao and L. Dong, "Microblower-based microfluidic pump," Sensors and Actuators, A: Physical, vol. 253, pp. 27-34, 2017.

[8] "Microfluidic Definitions and Advantages," Fluigent Smart Microfludics. [Online]. [Accessed 2019].

[9] L. Hung, R. Lin and A. Lee, "Rapid microfabrication of solvent-resistant biocompatible microfluidic devices," Lab on a Chip, vol. 8, no. *6*, pp. 983-987, 2008.

[10] K. Liu and Z. H. Fan, "Thermoplastic microfluidic devices and their applications in protein and DNA," Analyst, vol. 136, pp. 1288-1297, *2011*.

[11] M. Tehranirokh, A. Z. Kouzani, P. S. Francis and J. R. Kanwar, "Microfluidic devices for cell cultivation and proliferation,*" Biomicrofludics,* vol. 7, 2013.

[12] S. Wu, J. Jeffet, A. Grunwald, H. Sharim, N. Gilat, D. Torchinsky, Q. Zheng, S. Zirkin, L. Xu and Y. Ebenstein, "Microfluidic DNA combing for parallel singlemolecule analysis," *Nanotechnology,* vol. 30, no. 4, 2019.

[13] E. Carrilho, A. W. Martinez and G. M. Whitesides, "Understanding Wax Printing: A simple micropatterning process for Paper-Based Microfluidics," *Analytical Chemistry,* vol. 81, pp. 7091-7095, 2009.

[14] A. Folch, Introduction to BioMEMS, Boca Raton, FL: CRC Press, 2013, pp. 1-.

[15] Potomac, "Custom Microfluidic Chips," [Online]. Available: https://www.potomac-laser.com/project-gallery/microfluidic-chip-fabrication-2/. [Accessed 2019].

[16] Syntec Optics, "PDMS Microfluidics," [Online]. Available: https://syntecoptics.com/polymer-optics-applications/pdms-microfluidics/. [Accessed 2019].

[17] "MEMS," Engineering and Technology History Wiki , 12 April 2017. [Online]. Available: https://ethw.org/MEMS. [Accessed 2019].

[18] A. W. Martinez, D. S. T. Phillips, D. M. J. Butte and G. M. Whitesides, "Patterned Paper as a Platform *for Inexpensive, Low Volume, Portable* Bioassays," Angewandte, vol. 46, no. 8, pp. 1318-1320, 2007.

[19] M. Kim, D. Ha and T. Kim, "Cracking-assisted photolithography for mixed-scale patterning and nanofluidic applications," Nature Communications, vol. 6, 2015.

[20] H. R. Fok and T. N. Jackson, "Self-Aligned Electrodes on SU-8 Negative Photoresist Pedestals," JOURNAL OF MICROELECTROMECHANICAL SYSTEMS, vol. 23, no. 3, 2014.

[21] P. Kim, K. W. Kwon, M. C. Park, S. H. Lee, S. M. Kin and K. Y. Suh, "Soft Lithography for Microfluidics: a *Review," Biochip* Journal, vol. 2, no. 1, pp. 1-11, 2008.

[22] A. Ziyara, F. Sucularlı, C. Varol, O. Totuk and E. Yildirim, "Optimization of Hot Embossing Process for Fabrication of Microfluidic Devices.," in *8th Engineering and Technology Symposium*, Cankaya University, Ankara, 2015.

[23] B. S. Rupal, E. A. Garcia, C. Ayranci and A. J. Qureshi, "3D Printed 3D-Microfluidics: Recent Developments and Design Challenges," *Integrated Design and Process Science,* vol. 22, no. 1, pp. 5-20, 2018.

[24] K.Adamski, W.Kubicki and R.Walczak, "3D Printed electrophoretic lab-on-chip for DNA separation," Procedia Engineering, vol. 168, pp. 1454-1457, 2016.

[25] A. Urrios, C. Parra-Cabrera, N. Bhattacharjee, A. Gonzalez-Suarez, L. Rigat-Brugarolas, U. Nallapatti, J. Samitier, C. Deforest, F. Posas, J. Garcia-Cordero and A. Folch, "3D-printing of transparent bio-microfluidic devices in PEG-DA," *Lab on a Chip,* vol. 16, no. 12, pp. 2287-2294, 2016.

[26] Y. K. Hahn, D. Hong, J. H. Kang and S. Choi, "A Reconfigurable Microfluidics Platform for Microparticle Separation and Fluid Mixing," micromachines, vol. 7, *no. 8, 2016.*

[27] C. M. B. Ho, S. H. Ng, K. H. H. Li and Y.-J. Yoon, "3D Printed Microfluidics for Biological Applications," Royal Society of Chemistry, vol. 15, *no. 18,* pp. 3627-3637, 2015.

[28] D. N. Bhattacharjee, D. C. Parra-Cabrera, D. Y. T. Kim, A. Kuo and P. A. Folch, "Desktop-Stereolithography 3D-Printing of a Poly(dimethylsiloxane)-based Material with Sylgard-184 Properties,*" Advanced Materials*, vol. 30, no. 22, 2018.

[29] J. Warner, P. Soman, M. T. Wei Zhu and S. Chen, "Design and 3D Printing of Hydrogel Scaffolds with Fractal Geometries," ACS Biomaterials Science and Engineering, vol. *2,* no. 10, pp. 1763-1770, 2016.

[30] W. Chu, Y. Tan, P. Wang, J. Xu, W. Li, J. Qi and Y. Cheng, "Centimeter-Height 3D Printing with Femtosecond Laser Two-Photon Polymerization," *Advanced Materials Technologies,* vol. 3, no. 5, 2018.

[31] M. Syamsuzzaman, N. A. Mardi, M. Fadzil and Y. Farazila, "Investigation of layer thickness effect on the," Materials Research Innovations, vol. 18, 2014.

[32] W. Su, B. S. Cook, Y. Fang and M. M. Tentzeris, "Fully inkjet-printed microfluidics: a solution to low-cost rapid three-dimensional microfluidics fabrication with numerous electrical and sensing applications," *Scientific Reports,* vol. 6, 2016.

[33] S. Ge, L. Zhang and J. Yu, "Paper-based microfluidic devices in bioanalysis: how far have we come?," Bioanalysis, vol. 7, no. 6, pp. 633-636, 2015.

[34] G. Sriram, M. P. Bhat, P. Patil, U. T. Uthappa, H.-Y. Jung, T. Altalhi, T. Kumeria, T. M. Aminabhavi, R. K. Pai, Madhuprasad and M. D. Kurkuri, "Paper-based microfluidic analytical devices for colorimetric detection of toxic ions: A review," *Trends in Analytical Chemistry,* vol. 93, pp. 212-227, 2017.

[35] C. Xi, C. Jin, Z. Hui-Yan, W. Fu-Bing, W. Fang-Fang, J. Xing-Hu and H. Zhi-Ke, "Colorimetric Detection of Alkaline Phosphatase on Microfluidic Paper-based Analysis Devices," *Chinese Journal of Analytical Chemistry,* vol. 44, no. 4, pp. 591-596, 2016.

[36] X. Li, D. R. Ballerini and W. Shen, "A perspective on paper-based microfluidics: Current status and future trends," Biomicrofluidics, vol. 6, 2012.

[37] Z. Nie, F. Deiss, X. Liu, O. Akbulut and G. M. Whitesides, "Integration of paper-based microfluidic devices with commercial electrochemical readers," Lab on a Chip, *vol. 10, pp. 3163-3169, 2012.*

[38] V. Suresh, O. Qunya, B. L. Kanta, L. Y. Yuh and K. S. L. Chong, "Non-invasive paper-based microfluidic device for ultra-low detection of urea through *enzyme catalysis,*" Royal Society, vol. 5, 2018.

[39] J. Yu, L. Ge, J. Huang, S. Wanga and S. Ge, "Microfluidic paper-based chemiluminescence biosensor for simultaneous determination of glucose and uric acid," Lab on a Chip, vol. 11, pp. 1286-1291, 2011.

[40] J. L. Delaney, C. F. Hogan, J. Tian and W. Shen, "Electrogenerated Chemiluminescence Detection in Paper-Based Microfluidic Sensors," Analyical Chemistry, *vol.* 10, pp. 1300-1306, 2011.

[41] W. Dungchai, O. Chailapakul and C. S. Henry, "A low-cost, simple, and rapid fabrication method for paper-based microfluidics using wax screen-printing," Analyst, vol. 136, no. *1, pp.* 77-82, 2011.

[42] S. G. R. s. T. R. &. S. p. Rajesh Ghosh, "Fabrication of laser printed microfluidic paper-based analytical devices (LP-µPADs) for point-of- *care* applications," Scientific Reportd, vol. 9, 2019.

[43] Y. Lu, W. Shi, J. Qin and B. Lin, "Fabrication and characterization of paper-based microfluidics prepared in nitrocellulose membrane by Wax printing," *Analytical Chemistry,* vol. 82, no. 1, pp. 329-335, 2010.

[44] K. M. Koczula and A. Gallotta, "Lateral flow assays," Essays in Biochemistry, vol. 60, no. 1, pp. 111-120, 2016.

[45] E. B. Bahadır and M. K. Sezgintürk, "Lateral flow assays: principles, designs and labels," Trends in Analytical Chemistry, vol. 82, pp. 286-306, 2016.

[46] "Understanding Pregnancy Tests: Urine & Blood," American Pregnancy Association, [Online]. Available: https://americanpregnancy.org/getting-pregnant/understanding-pregnancy-tests/. [Accessed 13 September 2019].

[47] B. M. Jayawardane, S. Wei, I. D. McKelvie and S. D. Kolev, "Microfluidic paper-based analytical device for the determination of nitrite and nitrate," *Analytical Chemistry,* vol. 86, no. 15, pp. 7274-7279, 2014.

[48] C. Liu, Y. Li and B.-F. Liu, "Micromixers and their applications in kinetic analysis of biochemical reactions," Talanta, vol. 205, 2019.

[49] A. R. Rezk, A. Qi, J. R. Friend, W. H. Li and L. Y. Yeo, "Uniform mixing in paper-based microfluidic systems using surface acoustic," *Lab on a Chip,* vol. 12, pp. 773-779, 2012.

[50] "PubChem," [Online]. Available: https://pubchem.ncbi.nlm.nih.gov/. [Accessed 2019].